Republic of Iraq

Ministry of Higher Education and Scientific Research

University of Babylon

College of Education for Pure Sciences

Department of Physics

Fabrication of Iron Oxide Nanofilms from Thermally Evaporated Iron after Heat Treatment: Structural and Optical Properties

A thesis
Submitted to the Council of the College of Education for Pure Sciences, University of Babylon in Partial Fulfillment of the Requirements for the Degree of Master in Education / Physics

by

Shaymaa Abdulaali Mukheef Obeis

B.Sc. in Physics
(University of Babylon 1999)

Supervised by

Prof.Dr.Fouad Sh. Hashim **Prof.Dr.Khalid Haneen Abass**

2022 A.D. 1443 A.H.

بِسْمِ اللَّهِ الرَّحْمَنِ الرَّحِيمِ

(لَقَدْ أَرْسَلْنَا رُسُلَنَا بِالْبَيِّنَاتِ وَأَنزَلْنَا مَعَهُمُ الْكِتَابَ وَالْمِيزَانَ لِيَقُومَ النَّاسُ بِالْقِسْطِ ۖ وَأَنزَلْنَا الْحَدِيدَ فِيهِ بَأْسٌ شَدِيدٌ وَمَنَافِعُ لِلنَّاسِ وَلِيَعْلَمَ اللَّهُ مَن يَنصُرُهُ وَرُسُلَهُ بِالْغَيْبِ ۚ إِنَّ اللَّهَ قَوِيٌّ عَزِيزٌ)

صَدَقَ اللهُ العَلِيّ العَظيم

[الحديد:25].

Supervisor's certificate

We certify that this thesis entitled " **Fabrication of iron oxide nanofilms from thermally evaporated iron after heat treatment: structural and optical properties** " was prepared by the student **(Shaymaa Abdulaali Mukheef)** under my supervision at the College of Education for Pure Sciences, University of Babylon as partial fulfillment of the requirement for the **Degree of Master in Education / Physics**.

Signature:

Name:.Dr. Fouad Shakir Hashim

Title: Professor

(Supervisor)

Date: / / 2022

Signature:

Name: Dr. Khaild Haneen Abass

Title: Professor

(Supervisor)

Date: / / 2022

Head of the Department Certificate

In view of the available recommendations, I forward this thesis for debate by the examining committee.

Signature:

Name: Dr. Khaild Haneen Abass

Title: Professor

(Head of Physics Department

Date: / / 2022

Dedication

I dedicate the fruits of my humble labor:

For him who separates the darkness with the light of his message and illuminates the aspects of mercy on every living thing, our master Muhammad, may God .bless him and his family and grant them peace

To the one who encouraged me to persevere all my life, to the most prominent man in my life

(My dear father)

To the soul of the one who is higher and on it rest on the giving heart

(My mother, may God have mercy on her)

To the one who was my support and showed me my way

(My husband, Dr. Mohammed Hadi Al-Shammary)

To those who made an effort to help me and had support

(my sisters)

To my children, friends and colleagues

To all of them I dedicate this humble work

Shaymaa

Acknowledgments

Thank God for love

Alhamdulillah thank you

Praise be to God, please and obedience

Praise be to God always and forever

And prayers and peace be upon the most honorable messengers, our master Muhammad, and upon all his family and companions.

I would like to extend my thanks and appreciation to Prof. Dr. Fouad Shaker Hashem and Prof. Dr. Khaled Hanin Abbas for suggesting the topic of research and for their outstanding supervision and efforts. They have my sincere thanks and gratitude.

My thanks and appreciation to the Deanship of the College of Education for Pure Sciences - University of Babylon and to the Head of the Physics Department for giving them the opportunity and their scientific sponsorship and their desire to lend a helping hand and help me.

I extend my thanks and appreciation to my family for the suffering they have suffered with me throughout the period of preparing this letter, their stance with me and their support for me.

Last but not least, I extend my sincere thanks, appreciation and respect to the graduate students. I wish them more excellence and success.

Shaymaa

Abstract

In this study, thermal evaporation technique was used to prepare iron (Fe) nano films deposited on glass substrates, with thickness of 75 nm and with different annealing temperatures of 200°C, 300°C, and 400°C and different annealing time at 200 °C for 3 and 4 hours by thermal evaporation. From X-ray diffraction (XRD) analyses avowed the formation of hematite phase for crystalline tetragonal structure (γ-Fe_2O_3) and maghemite hexagonal crystal structure (α-Fe_2O_3). Annealing at different temperature and time in the presence of air leads to oxidation and reveal the different phases of iron oxide maghemite and hematite. The average crystallite size of Fe nanofilms increased with increasing annealing temperature and time. It increased from 15.12 nm as-deposited to 21.67 nm at 200°C for 4 hours. Atomic force microscope (AFM) images of iron oxide nanofilms showed a high surface homogeneity in which the distribution of crystalline granules is uniform which is evident from the convergence of the roughness and root mean square (RMS) values. The roughness and root mean square (RMS) values were increased from 1.1 nm and 1.43 nm as-deposited nanofilm to 8.35 nm and 10.6 nm annealed at 200 ^{o}C for 4 hours. Scanning electron microscope (SEM) images showed that the assemblies of nanoparticles in the form of a flowers are spread on the surface, which appeared in all the deposition glass samples, especially at a temperature of 200 ^{o}C. The optical properties results showed that the absorbance increases with increasing annealing temperature in the UV region and then reduces in the visible and NIR regions, while the transmittance reduce with increasing annealing temperature in the UV region and then increase in the visible and NIR regions. The optical measurement showed that the Fe nanofilms have allowed direct energy gap (E_g). The E_g

decreased with increasing annealing temperature and time respectively. It is decreased from 3.48 eV as-deposited to 3.33 eV at 400 ^{o}C for 2 hours and from 3.48 eV as-deposited to 3.40 eV at 4 hours for 200^{o}C. The optical constants such as absorption coefficient, extinction coefficient, refractive index and real and imaginary parts of dielectric constant also were studied.

Table of Contents

List of Tables

List of Figures

List of Symbols

Symbol	description
A_b	Absorption
E_g	Energy Gap
I_T	Transmitted Photon Intensity
I_o	Incident Photon Intensity
$R_e)$	Reflectance
n_c	Complex Refractive Index
ε_i	Imaginary Part
ε_r	Real Part
λ_{max}	Maximum Wavelength
a,c	Lattice Constant
A_b	Absorption
B	FWHM in radians
c	Light Velocity
D	Crystallize Size
d_{hkl}	Interplanar distance
E_g	Energy Gap
h	Plank's Constant
$h\upsilon$	Photon Energy
$h\upsilon$	Incident Photon Energy
K	Kelvin
k	Extinction Coefficient
m	Mass of the Material
N	Number of Crystals per Area
n	Refractive Index
N_L	Number of Layers
R	Distance Between the Substrate and the Boat
S	Micro Stresses
t	Film Thickness
T_m	Melting Temperature
T_r	Transmittance

α	Absorption Coefficients
δ_D	Dislocations
θ	Bragg's Angle
λ	Wavelength
ρ	*D*ensity of Material
υ	Incident Photon Frequency
ϑ	Velocity of Propagation

List of Abbreviations

Symbol	description
0D	Zero Deamination
1D	One Deamination
2D	Two Deamination
3D	Three Deamination
AFM	Atomic Force Microscope
bcc	Body Centered Cubic
C.B	Conduction Band
fcc	Face Centered Cubic
Fe_2O_3	Iron(III) Oxide
FWHM	Full width at half maximum
hcp	hexagonal close packed
Mo	Molybdenum
NPs	nanoparticles
PET	Polyethylene Terephthalate
PVD	Physical Vapor Deposition
RMS	Root Mean Square
RT	Room Temperature
SEM	Scanning Electron Microscope
V.B	Valence Band
XRD	X-Ray Diffraction
α-Fe	alpha iron

Chapter One

Historical Review

1.1.Introduction

The term "Thin Films" refers to a layer or many layers of atoms for a certain substance whose thickness is less than (1 μ) [1]. The majority of the physical properties of a thin film differ from those of its constituent elements [2]. In 1852, scientists (Grove & Bunsen) utilised (Chemical Reaction) to create these films, and in 1857, scientist (Faraday) utilised (Thermal Evaporation) to create a thin metal film [3]. Today, thin films are of great relevance due to the industries that employ them. These films have been used in various fields, including the production of (p-n) junctions, rectifiers, reflected and anti-reflected coatings, photographs, mirrors of two types, ordinary and thermally, integrated circuits, and optical communications such as light emitting diodes, detectors, and solar cells, etc. Based on the nature of the deposition process, thin oxide film deposition methods can be categorised into two groups: physical and chemical. Vacuum evaporation, a typical method of physical vapour deposition (PVD) for depositing coatings of pure materials to the surface of various objects, is one of the physical deposition processes. Coatings are typically nanometers thick for nanofilms or angstroms to microns thick for films and can be composed of a single material or numerous components in a layered structure[4].

At atmospheric pressure, iron has two distinct crystal structures: the body-centered cubic (bcc) and the face-centered cubic (fcc). The bcc α-phase is stable in the ground state, and at T=1184 K, α-Fe changes into fcc α-Fe, which is stable up to 1665 K. Iron reverts to the bcc phase (σ-Fe) above this temperature, which stays stable up to the melting temperature Tm = 1809 K. Because α-Fe and σ-Fe are isomorphic, they are typically not separated when discussing bcc Fe. Typically, steels with bcc and fcc structures are referred to as "ferrite" and "austenite" Iron's boiling point is around 3300K. A third type of

iron, with the structure of hexagonal close packing (hcp), can be stable under high pressures [5].

Iron oxides are iron- and oxygen-based chemical compounds. There are sixteen known iron oxides and oxyhydroxides, with rust, a type of iron(III) oxide, being the most well-known. Iron oxides and oxyhydroxides are abundant in nature and play crucial roles in numerous geological and biological processes. They are found in haemoglobin and are employed as iron ores, pigments, catalysts, and in thermite. It is a cheap and powerful pigment for use in paints, varnishes, and coloured concrete. Commonly accessible hues fall on the earthier end of the spectrum of yellow, orange, red, brown, and black [6].

Nanomaterials frequently exhibit innovative and unusual electrical, optical, magnetic, and chemical properties as compared to their bulk counterparts [7]. The specific applications of nanoparticles are determined by the nanomaterials in which they are involved. Nano materials are categorised as 'closely packed materials' and 'Nano dispersions' that include "nanostructured" materials, i.e., an isotropic material with a macroscopic composition consisting of compact Nano metre sized units, such as the fundamental replicating structural and functional elements [8].

There are eight well-known iron oxides in nature [9], of which magnetite (Fe_3O_4), maghemite (γ-Fe_2O_3), and hematite (α-Fe_2O_3) exhibit unique magnetic characteristics, polymorphic morphologies, and temperature-induced phase transitions. Magnetite and maghemite are suitable industrial and medical materials. Due to their unique magnetic, catalytic, and biochemical capabilities, both are superior to other iron oxides from a reusability standpoint [10, 11]. The (1-100 nm) diameter iron oxide nanoparticles utilised in magnetic data storage, bio sensing, drug-delivery, etc. [12-15]. The ratio of surface area to volume in nanoparticles (NPs) increases dramatically. This gives NPs in solutions a significantly better binding capacity and superior dispersibility.

Magnetic nanoparticles of diameters between (2-20) nm exhibit super Paramagnetism, meaning that their magnetization is zero in the absence of an external magnetic field and they can be magnetised by an external magnetic source. This feature increases the aqueous stability of magnetic nanoparticles [16].Magnetite possesses an inverted spinel crystal structure, with oxygen producing a face-centered cubic crystal system. All tetrahedral sites in magnetite are occupied by Fe^{+3}, while octahedral sites are inhabited by both Fe^{+3} and Fe^{+2}.

Maghemite differs from magnetite in that all or the majority of the iron is in the trivalent form Fe^{+3} and action vacancies are present at the octahedral sites. Maghemite has a cubic unit cell with 32 (O) ions, $^{211/3}Fe^{+3}$ ions, and $2^{2/3}$ vacancies in each cell. The activities are randomly distributed among the eight tetrahedral and sixteen octahedral locations [17]. Co-precipitation [18], High-temperature thermal decomposition [19], Hydrothermal and solvothermal synthesis [20], Sol–gel reactions and polyol method [21], Micromemulsim [22], Sonolysis or sonochemical method [23], Microwave-assisted synthesis, [24], Biosynthesis [25], electrochemical methods [26], flow injection synthesis [27], and aerosol/vapor methods [28] were used to prepare (FeO).

As previously stated, Fe_2O_3 nanoparticles have a wide variety of applications, including terabit magnetic storage devices, catalysis, sensors, super paramagnetic relaxometry, high-sensitivity biomolecular magnetic resonance imaging, magnetic particle imaging, magnetic fluid hyperthermia, separation of biomolecules, and targeted drug and gene delivery for medical diagnosis and therapeutics. For these uses, the nanoparticles must be coated with agents such as long-chain fatty acids and alkyl-substituted amines. They have been utilised in dietary supplement compositions. Due to their superparamagnetic features and prospective uses in numerous industries, [29] they have gained a great deal of attention.

1.2 Literature Review

This literature review analyses the literature relevant to the planned work and provides an overview of some studies. Fundamental and practical factors drive interest in nanoscale iron oxides. Iron(III) oxide (ferric oxide, Fe_2O_3) is polymorphic and one of the most fascinating iron oxides. Its biochemical, magnetic, catalytic, and other qualities make it appropriate for certain technical and biomedical applications. High-temperature treatment is a vital step in most iron(III) oxide syntheses, although it typically promotes polymorphous transformations that generate unwanted Fe_2O_3 polymorph mixes..

Machala L.*et al.,* in (2011) [30], discussed mechanism and kinetics of Fe_2O_3 polymorphous transformations depend on intrinsic material properties (polymorph structure, particle size, particle morphology, surface coating, particle aggregation, particle incorporation within a matrix) and external parameters of synthetic and/or natural conditions such as temperature, atmosphere, and pressure. High-temperature, high-pressure Fe_2O_3 reactions. These polymorphous changes' analytical tools.

Mohammad .*et al.,* in (2012) [31], reported that the reactive evaporation of iron in an oxygen atom-sphere produced thin coatings of hematite (α-Fe_2O_3). Substrates with and without heat were used to deposit the films. A polycrystalline structure composed of nano-crystallites was discovered by structural investigation utilising X-ray diffraction. As substrate heating increased, the grain size of the films rose significantly, according to atomic force microscopy (AFM). The optical parameters of the films, such as the refractive index, extinction coefficient, absorption coefficient, and band gap, were determined using spectrophotometric techniques. Films applied to

unheated substrates had refractive indexes between (1.7-2.2) whereas films applied to heated substrates had refractive indexes between (2.3-2.9). Direct and indirect band gaps were present in the films. According to the substrate temperature, the direct band gap was (2.18 eV) and the indirect band gap was (1.82-1.96 eV).

Yucheng. *et al.,* in (2013) [32], High-yield, low-cost heat evaporation-induced anhydrous method to manufacture Fe_3O_4 nanoparticles with graphene as an improved anode for lithium ion batteries. (10-20) nm Fe_3O_4 nanoparticles are tightly attached to conductive graphene sheets and act as spacers. For example, the Fe_3O_4/graphene composite has high retention capacity of 868 mA/g up to 100 cycles at a current density of 200 mA/g and 539 mA/hg up to 200 cycles at a current density of 1000 mA/g. The straightforward method prepares anode materials for lithium ion batteries.

Eunice . *et al.,* in (2015) [33] , Hematite (α-Fe_2O_3), magnetite (Fe_3O_4), and maghemite (γ-Fe_2O_3) are polymorphs of iron oxide. Nanoparticulate solid propulsion materials, including hematite and maghemite, decompose ammonium perchlorate well. Their particle size, more active sites, and high surface area facilitate gas adsorption during thermal oxidation processes, boosting their catalytic effect. Metallic iron nanoparticles can be made by co-precipitation, sol-gel, microemulsion, or thermal decomposition. Although the literature contains information on these synthetic processes, it lacks information on nanoparticulate oxides and their characterisation.

Diana and Yong 2016 [34], reported Iron oxide nanoparticles were produced by precipitating sodium hydroxide and ammonium hydroxide in isobutanol. Isobutanol acted as a surfactant during the synthesis. The nanoparticles were calcined for 100 minutes to five hours between 300 and 600 ^oC. FTIR (Fourier-transform infrared) and XRD (X-ray diffraction) analysis of the samples showed the synthesis of γ-Fe_2O_3 (maghemite) from Fe_3O_4

(magnetite) during calcination at 300°C. SEM was used to investigate the morphology and particle size (scanning electron microscope). 11–22 nm nanoparticles produced with 0.09M ferrous chloride demonstrated superparamagnetic characteristics. α-Fe_2O_3 nanoparticles were produced with ferrous chloride and ammonium hydroxide at 75^{o}C and calcined at 530^{o}C for 2 hours (hematite).

Yazirin, C. *et al.*, in (2017) [35] , examine the phase and shape of iron oxide (Fe_2O_3) powder that has been sintered for 1 hour, 2 hours, and 3 hours with ethylene glycol as a solvent. The instruments used for characterization were XRD, SEM-EDX, and FTIR. XRD research revealed that the Fe_2O_3 sintered for one hour had the smallest crystallite size, measuring 21.05 nm in diameter. During the XRD test, the X-ray beam was directed directly at the grain being evaluated. SEM research revealed that Fe2O3 sintered for one hour generated the best results due to its crystallite size of 12.36 nm and nanosphere-like form; the period of sintering had a significant impact on the grain size of iron oxide (Fe_2O_3). According to the results of the elemental composition analysis, the longer the sintering process, the higher the concentration of oxygen, but the lower the concentration of iron.

Suturin . *et al.*, in (2018) [36], Epitaxial iron oxides on GaN(0001) surface were polymorphized. Fe_3O_4, γ-Fe_2O_3, ε-Fe_2O_3 and α-Fe_2O_3 have been stabilised using single target Laser MBE technology. It is possible to fabricate single phase layers by varying the substrate temperature, buffer gas composition, and pressure. On GaN, the X-ray diffraction (XRD), atomic force microscopy (AFM), as well as the electrical and magnetic properties of single phase iron oxide epitaxial films have been investigated.The electrical, magnetic, and X-ray diffraction properties of single phase iron oxide epitaxial films on GaN have been examined.

Natarajan .*et al.*, in (2019) [37]. described the structural and magnetic properties of magnetic iron oxide nanoparticles (MIONPs), specifically

magnetite, maghemite, and hematite, followed by essential synthetic methods that can be used for biological applications. In vivo cytotoxic effects and surface modifications to eliminate cytotoxicity wer also studied. Surface-modified MIONPs are used in medical and industrial platforms for global health.

Coduri M. *et al.*, in (2020) [38] investigated the structural and magnetic changes caused by shrinking maghemite-Fe_2O_3 crystals. XRD and TEM crystal sizes agreed. Except for Aldrich, which has a size distribution of up to 100 nm, the other three specimens studied have a size distribution of 10–15 nm for Iolitec, 4–5 nm for P520, and 2 nm for P200.

Khadayeir *et al.*, in (2022) [39], α-Fe_2O_3 thin layer was produced on a glass substrate using chemical spray pyrolysis at 450°C to examine the effect of cold plasma on self-cleaning and antibacterial capabilities. XRD, FESEM, EDS, and AFM were utilised to examine α-Fe_2O_3 thin layers before and after plasma injection. Wetting and antibacterial properties of iron oxide (hematite) thin film were investigated in the presence of gram-negative and gram-positive bacteria before and after plasma injection. Plasma exposure α-Fe_2O_3 thin film affects shape, self-cleaning, and antibacterial properties.

1.3 The Aim of Work

The aims of this work is to prepared the iron oxide nanofilms from iron using thermal evaporation method after subjected to different annealing temperature and time. Other objectives can be achieved through this research such as study of structural , morphological and optical properties of the prepared devices for some application.

Chapter Two

Theoretical Consideration

2.1 Introduction

This chapter cover the general description of the theoretical side-parts of the structural, morphological, optical measurements and gives a satisfactory review including all the relations, scientific explanations which are used in this thesis.

2.2 Structure of Iron (Fe)

Iron's atomic weight is 56, compared to Al's 27, Pb's 207, and C's 12. At normal temperature, iron's atoms form a body-center cubic lattice (bcc). The smallest recurring 3D pattern is a cube with an atom at each corner and one in the middle. Figure (2.1(a)) shows ferrite [40].

If iron is heated to 910°C, it adopts a pattern in which one atom sits in the middle of each planar square of the former bcc pattern. Face centre cubic is the new pattern (fcc). Austenite figure (2.1(b)) [41].

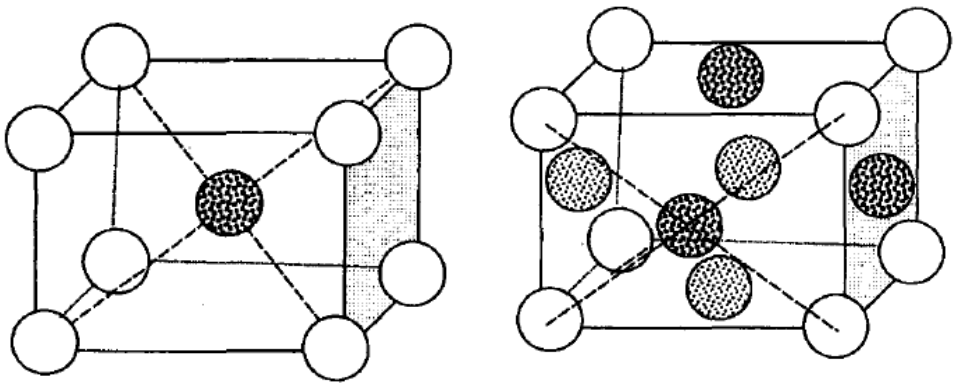

(a) **(b)**

Fig.(2.1) Structure of Iron: (a) Body center cubic (bcc)m (b) face center cubic (fcc) [40,41].

2.3 Iron Oxide

The inorganic chemical known as iron oxide can be found in many different forms in nature. The most frequent chemical formulas for iron oxide nanoparticles are Fe_3O_4 as magnetite and γ-Fe_2O_3 (maghemite) and α-Fe_2O_3. Both magnetite and maghemite have features that make them suitable for use in biomedicine, including strong saturation magnetization and superparamagnetic behaviour. Calcination in air changes magnetite (Fe_3O_4) into maghemite (Fe_2O_3) by the following chemical reaction: $4\ Fe_3O_4 + O_2 \rightarrow 6\ \gamma\text{-}Fe_2O_3$.

Iron cations are found in either octahedral or tetrahedral interstitial positions, and the crystal structure of all three iron oxides may be characterised in terms of closely packed planes of oxygen anions. Both magnetite and maghemite have the same structure, but maghemite contains cationic vacancies in one-third of the octahedral sites, whereas magnetite has Fe^{3+} in all of the tetrahedral sites and both Fe^{3+} and Fe^{2+} in the octahedral sites [42]. Magnetite has a spinel structure. The degree of vacancy ordering decreases with decreasing particle size, and there is no vacancy ordering in maghemite smaller than about 20 nm as mentioned by Haneda and Morrish [43] .

Maghemite (γ-Fe_2O_3) is appears either in a cubic structure with the space group P4332 with the presence of disturbances in the crystal structure is partial iron voids or in the structure of tetragonal with group of space P41212 with full site ordering and has c/a = 3. This means that the cubic structure is partly irregular and the tetragonal structure is completely regular, therefore, the structure that appears with the space group P41212 is already more stable, and this stability appears as a result of favorable electrostatic contribution. Therefore, this structure exhibits the highest

possible degree of uniformity in regard to the distribution of cations and vacancies [44].

Hematite (α-Fe_2O_3) is the most common form of iron oxide found in rocks and soils. It is also the most stable form of iron oxide, exhibiting ferromagnetic properties and high saturation magnetization [42,43].

Hematite is the earliest known of the iron oxides. As illustrated in figure(2.2), iron(III) cations, which are present in hematite, fill approximately two-thirds of the octahedral sites that are limited by the

nearly perfect hexagonal close-packed oxygen lattice.. hexago, As shown in figure (2.2) [45].

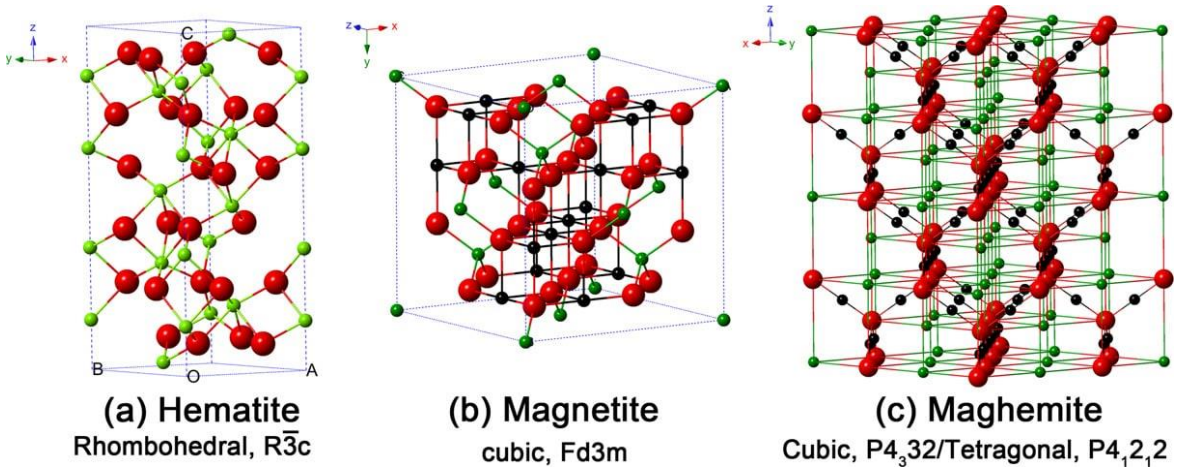

Fig.(2.2) Hematite, magnetite, and maghemite all have the same crystal structure. The black ball is Fe2+, the green ball is Fe3+, and the red ball is O2.

Table (2-1) summarizes the most prevalent iron oxide's physical and magnetic properties (2-1).

Table (2-1) Iron oxide's physical and magnetic properties

Property	Oxide		
	hematite	magnetite	maghemite
Molecular formula	α-Fe_2O_3	Fe_3O_4	γ-Fe_2O_3
Density(g/cm^3)	5.26	5.18	4.87
Melting point (C)	1350	1583-1597	-
Type of magnesium	Weakly ferromagnetic or antiferromagnetic	Ferromagnetic	Ferrimagnetic
Crystallographic system	Rhombohedral , hexagonal	Cubic	Cubic or tetrahedral
Lattice parameter (nm)	a=0.5034, c=1.375 (Hexagonal) a_{Rh}= 0.5427, α=55.3° Rhombohedral	α=0.8396°	a=0.5034, c=1.375 (Hexagonal) a_{Rh}= 0.5427, α=55.3° Rhombohedral
Energy gap (eV)	0	0	0

2.4 Nanomaterial's

The term "nanomaterial" is used to describe materials in which a single unit is small in size (in at least one dimension) compared to the typical definition of "nanoscale," which is defined as the "length range approximately from 1 nm to 100 nm." This covers nanoobjects in their entirety [47].

Utilizing recent advancements in materials metrology and synthesis that have been created in support of microfabrication research, the research carried out by Nanomaterial brings a materials science-based approach to the field of nanotechnology. Materials that have structure on the nanoscale typically exhibit properties that are one of a kind in the optical, electrical, thermophysical, or mechanical realms [48-50]. Nanomaterials are inching their way toward commercialization [51] and are starting to appear as potential commodities [52].

Both the synthesis of nanomaterials and the manufacturing of nanostructures can be done in either a top-down or bottom-up fashion. Both methods are self-evidently viable. The two different strategies are depicted in figure (2.3). Milling or attrition is an example of a typical top-down approach used in the production of nanomaterials [53-55].

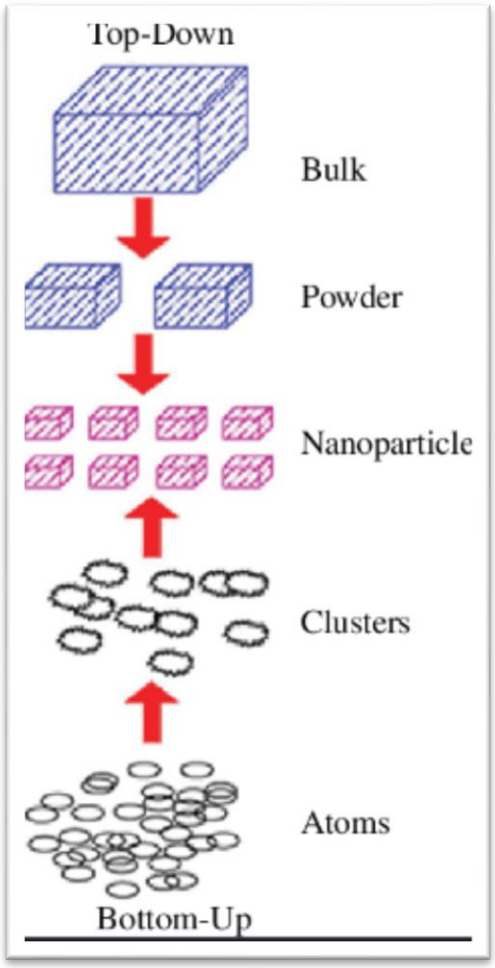

Fig. (2.3): Schematic representation of the 'bottom up' and 'top down' synthesis processes of nanomaterials [55]

The number of dimensions that are in the nano range (less than 100 nanometers) is used to classify nanomaterials [56], as illustrated in Figure (2.4) [57]:

1. 0D nanomaterials have no dimensions that are greater than 100 nanometers, meaning that all of the dimensions are contained inside the

nanoscale. The nanoparticle serves as the most typical example for this classification. Nanoparticles can have a variety of different structures, including crystalline or amorphous, metallic or ceramic, or polymeric.

2. One-dimensional nanomaterials have at least one dimension that falls within the nano range. This results in materials having a single dimension at the nanoscale and taking the form of needles. Nanoplatelets, nanorods and nanoclays, are examples of several types of 1D nanomaterials.

3. Nanomaterials with two dimensions in the nano range are referred to as 2D. Nanofibers, nanotubes, nanorods, and whiskers are examples of several types of 2D nanomaterials. nanosheets made of carbon are an excellent example of a 2D nanomaterial.

4. All three dimensions are present in 3D nanomaterials. 3D nanomaterials include nanogranules and nanoclays.

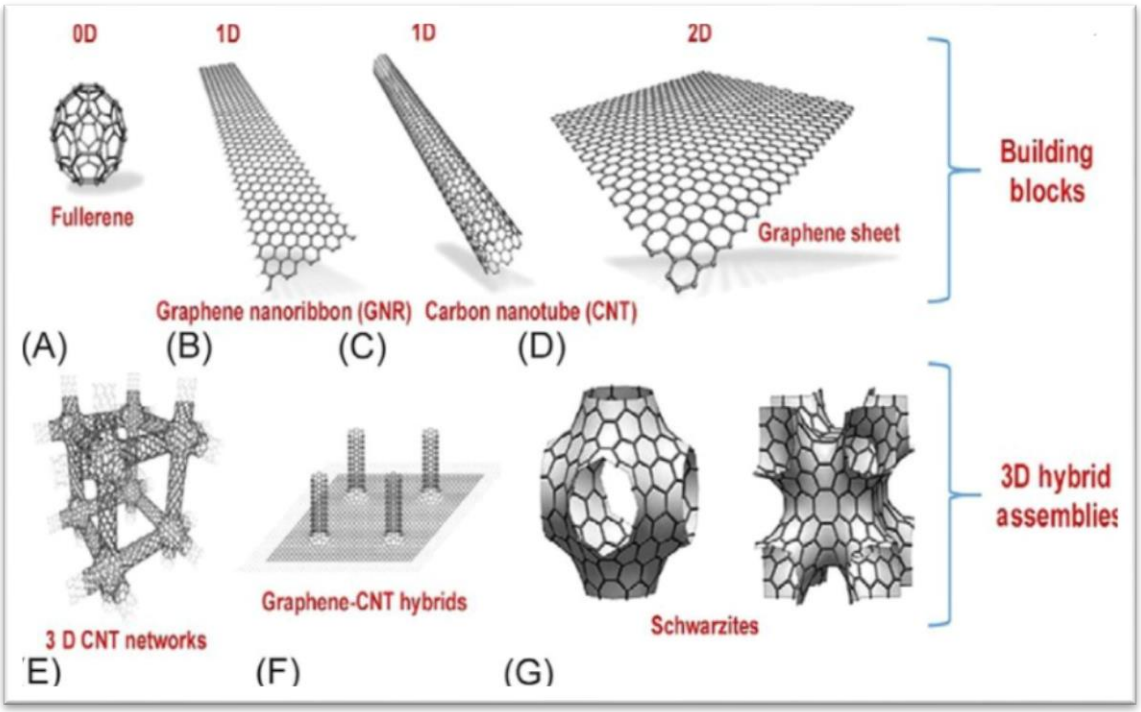

Fig.(2.4): Classification of nanomaterials (a) 0D nanomaterials (b) 1D nanomaterials (c) 2D nanomaterials (d) 3D nanomaterials [57]

2.5 Thermal Evaporation Techniques

Evaporation is a technology that is frequently used for the deposition of thin films. Evaporation of the source substance takes place in a vacuum. The vacuum makes it possible for vapour particles to move directly to the target item (substrate), where they can then return to a solid state after having been in a vapour state. In addition to its usage in microfabrication, evaporation is also put to use in the production of macro-scale goods, such as the metallized plastic sheet illustrated in figure (2.5).

Figure (2.5) Thermal Evaporation in a resistive heated boat [58]

The manufacture of aluminized PET film packaging film using a roll-to-roll web system is a significant example of an evaporative process. Since it is possible to deposit a thinner coating of aluminium on this material for a lower cost than a thicker layer, the aluminium layer in this material is frequently not thick enough to be totally opaque. Aluminum serves primarily to insulate the product from the external environment by forming a barrier that prevents the passage of light, oxygen, or water vapour. This is the primary function of the aluminium.

As can be seen in figure (2.6), evaporation is a technique that is frequently employed in microfabrication to deposit metal films [58-60].

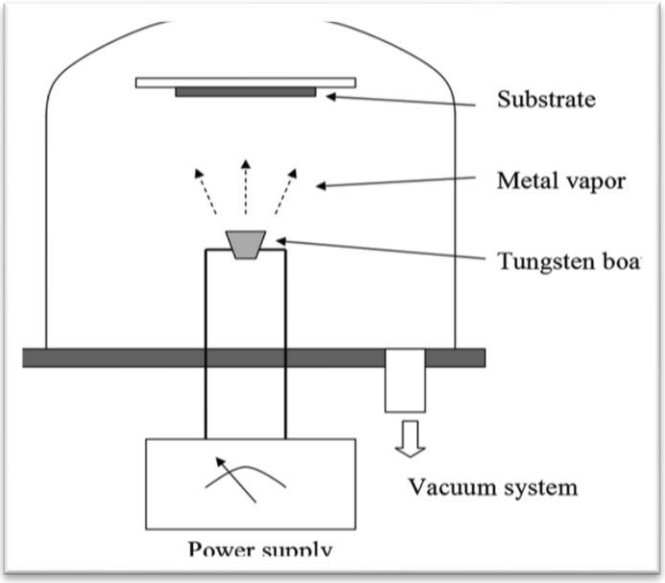

Figure (2.6) Resistive Heating[60]

Briefly the advantages of induction-heated thermal [59] :

1. A low level of contamination in the thin films that were deposited.

2. An improvement in the ability to control the rate of deposition.

3. It is possible to add larger charges into each deposition run.

2.6 Structural and Morphological Properties

In order to get exact information about the crystal structure, surface morphology, particle size etc. The structural properties of the films were studied by X- ray diffraction (XRD). The morphology of surface thin films was studied by field emission scanning electron microscopy (FE-SEM). The mechanical imaging was studied by atomic force microscopy (AFM).

2.6.1 X- Ray Diffraction (XRD)

The X-ray diffraction technique (XRD) is an effective method for determining the crystal structure and lattice parameters. The Bragg

spectrometer is an essential piece of equipment for any investigation of this nature. Bragg's law is the name given to the mathematical formula that describes the angle at which a beam of X-rays with a specific wavelength diffracts from the surface of a crystalline material. This formula was found by William H. Bragg and W. Lawrence Bragg. [61].

$$\mathbf{2d_{hkl}\sin\theta = \lambda} \qquad (2.1)$$

Wherever, λ is wavelength of the X-ray, θ is Bragg diffraction angle of the XRD peak in degree (scattering angle), and d_{hkl} = d/n is inter-planar distance, as shown in Figure (2.7).

The deposit size is determined from the FWHM of the most intense diffraction line using Debye Scherrer's formula [62].

$$D_S = \mathbf{K}\,\lambda / \beta \cos\theta \qquad (2.2)$$

In this equation, K is a constant regardless of the structure type, and D_S is the crystallite size, β is (FWHM) in radians.

The c-lattice constant of a hexagonal structure might deviate if the micro stresses (**S)** in the lattice are stretched or compressed during the formation of thin films [62]. Based on the relationship, this micro strain can be determined [63].

$$S = \beta \cos\theta / 4 \qquad (2.3)$$

Dislocation density (δ_D) is the number of dislocations per unit volume of crystalline material. [64]

$$\delta_D = \frac{1}{D_S^2} \qquad (2.4)$$

Microstructural factors like film texture can control electrical characteristics of polycrystalline thin films[65]. According to percolation

theory, the number of crystals per area (N) depends on film thickness (t). [66]:

$$\mathbf{N} = \frac{t}{D_S^3} \qquad (2.5)$$

The number of layers can be calculated from [66] :

$$\mathbf{N}_l = \frac{t}{D_s} \qquad (2.6)$$

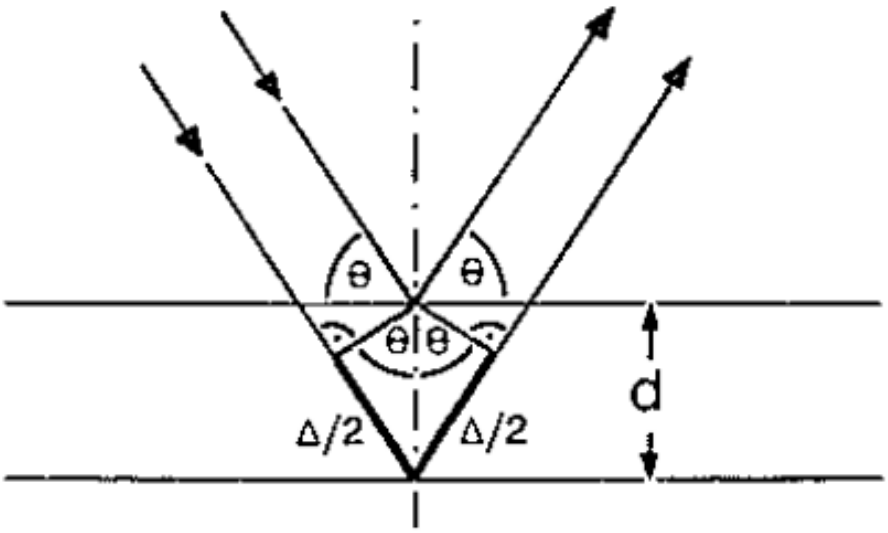

Figure (2.7) Bragg diffraction[61].

2.6.2 Scanning Electron Microscopy (SEM)

SEM is a common tool in material research labs. Electrons are employed instead of light waves to observe a specimen's microstructure. Because electrons are accelerated to high energies (KeV), their wavelengths are tiny and their resolution is high. SEM is used to measure gate widths, gate oxides, film thicknesses, fabrication details, minor contamination feature shape, and elemental composition as shown in Figure (2.8) [67,68].

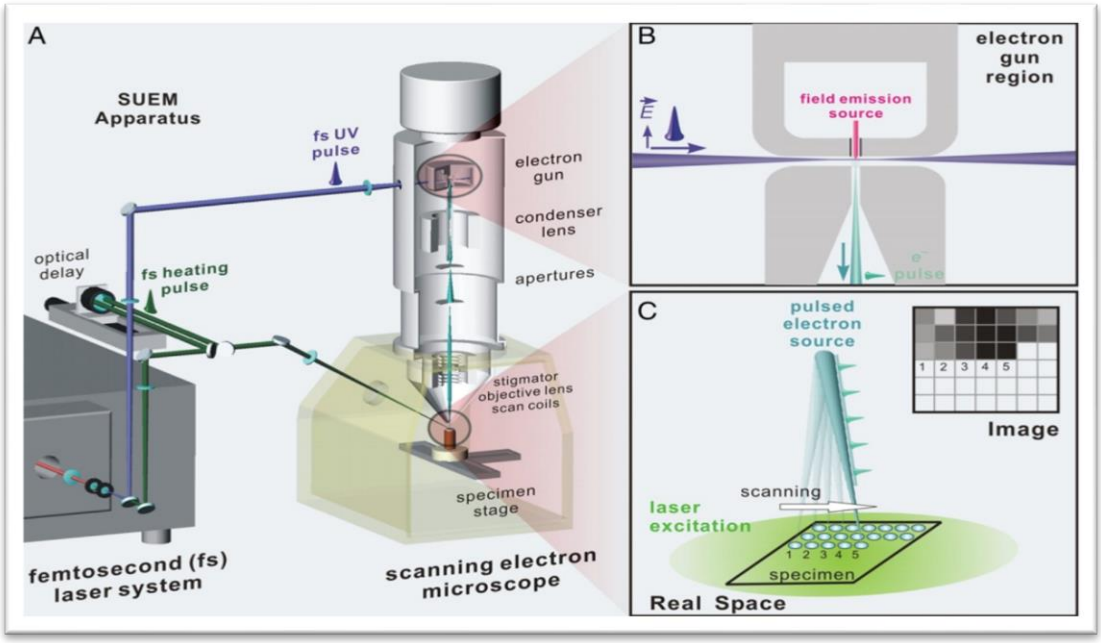

Fig.(2.8) Scanning Electron Microscopy (SEM)[68]

2.6.3 Atomic Force microscopy (AFM)

AFM evaluates surface topography and physical characteristics with a sharp probe. The probe is sharpened so it can interact with the surface's force fields. The probe is scanned so that forces remain constant [69]. The surface image is then recreated by tracking the probe's precise motion as it scans across it. The probe is scanned raster-style. (AFM) analyses in order to find the average grain size and surface topography at atomic scale of the samples, as shown in Figure (2.9) [70].

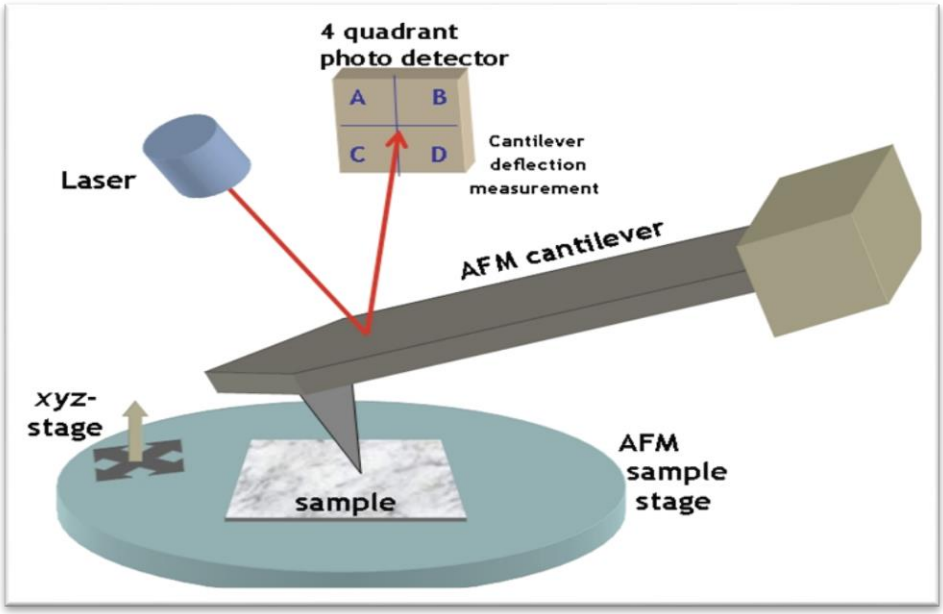

Figure (2.9) Atomic Force Microscopy[70]

2.7 Optical Properties

Many optical qualities are related to electrical and electronic properties. Intrinsic effect affects semiconductor optical characteristics. Depending on the placement of the valence band (V.B.) and conduction band (C.B.) in the band structure, electron-hole pair production occurs directly or indirectly. Visible transparency varies on deposition process and thickness [71,72]. Fundamental absorption involves the movement of electrons from the valence to the conduction band, resulting in a quick rise in absorption that can be utilized to calculate the semiconductor's energy gap [73].

The semiconductor absorbs energy photons (h υ) from the incident beam, where (h) is Plank's constant and (υ) is the input photon frequency.

If photon energy (h υ) is equal to or greater than energy gap (E_g), photon can interact with valence electron and generate electron–hole pair [74]. The incident photon's maximum wavelength (λ_{max}) is [75]:

$$\lambda_{max} = \frac{hc}{E_g} = \frac{1.24}{E_g\ (eV)} \qquad (2.7)$$

The intensity of the photon flux decreases exponentially with distance through the semiconductor according to Beer's law [76]:

$$\mathbf{I_T = I_o e^{-\alpha t}} \quad (2.8)$$

Where (I_o, I_T) represent the intensity of the incident and transmitted photons, (α) represents the absorption coefficients given in Eq. (2.3), which are defined as the number of photons absorbed per unit distance of the semiconductor, and (t) represents the thickness of the film. [77]:

$$\boldsymbol{\alpha = 2.303 \frac{A_b}{t}} \quad (2.9)$$

Where (A_b) is the absorption.

Direct and indirect radiation absorption lead to electronic transitions between the valence and conduction bands. Tauc equation describes transitions [78]:

$$\mathbf{(\alpha h\nu) = B(h\nu - E_g)^r} \quad (2.10)$$

For direct and indirect optical transitions, (hv) is the incident photon energy, and (r) is a constant constant that takes the values (1/2, 3/2, 2, and 3) depending on the material and the type of optical transition whether it is direct or indirect [79,80]. The optical constants are vital parameters since they describe the material's optical behaviour. The material's absorption coefficient is highly dependent on photon and band gap energies. If the absorption coefficient is large ($\alpha>10^4$), direct electronic transmission is conceivable [81]. Refractive index (n), extinction coefficient (k), real (ε_r) and imaginary (ε_i) dielectric constant parts.

complex refractive index (n_c) [74]:

$$\mathbf{n_c = n - ik} \quad (2.11)$$

It's connected to propagation velocity (ϑ) and light speed (c) by:

$$\boldsymbol{\vartheta = \frac{c}{n_c}} \qquad (2.12)$$

The refractive index is computed as follows [75]:

$$\boldsymbol{n = \left(\frac{4R_e}{(R_e-1)^2} - k^2\right)^{1/2} - \frac{(R_e+1)}{(R_e-1)}} \qquad (2.13)$$

Where (R_e) is the reflectance, which is calculated by using equation [82]:

$$\boldsymbol{R_e = 1 - T_r - A_b} \qquad (2.14)$$

Where (T_r) is the transmittance, (A_b) is the absorption.

The extinction coefficient is defined as [76]:

$$\boldsymbol{k = \frac{\alpha\lambda}{4\pi}} \qquad (2.15)$$

Where (λ) is the incident radiation's wavelength. The real part (ε_r) and imaginary part (ε_i) of dielectric constant can be calculated by using the following equation [83]:

$$\boldsymbol{(n - ik)^2 = \varepsilon_r - \varepsilon_i} \qquad (2.16)$$

The real and imaginary dielectric coefficient can be written as in following equation [70]:

$$\boldsymbol{\varepsilon_r = n^2 - k^2} \qquad (2.17)$$

$$\boldsymbol{\varepsilon_i = 2nk} \qquad (2.18)$$

2.7.1 Ultraviolet - visible spectroscopy or Ultraviolet-visible

UV-Vis or UV/Vis spectrophotometry is absorption or reflectance spectroscopy in the ultraviolet-visible spectrum. It uses visible and near-UV/NIR light. The substances' visual absorption or reflection impacts their apparent hue. Here, molecules undergo electronic transformations.

Absorption spectroscopy is complementary to fluorescence spectroscopy since fluorescence measures ground-to-excited state transitions[84].

Molecules with π-electrons or non-bonding electrons (n-electrons) can absorb UV or visible light to excite these electrons to higher anti-bonding orbitals[85] as shown in Figure (2.10).

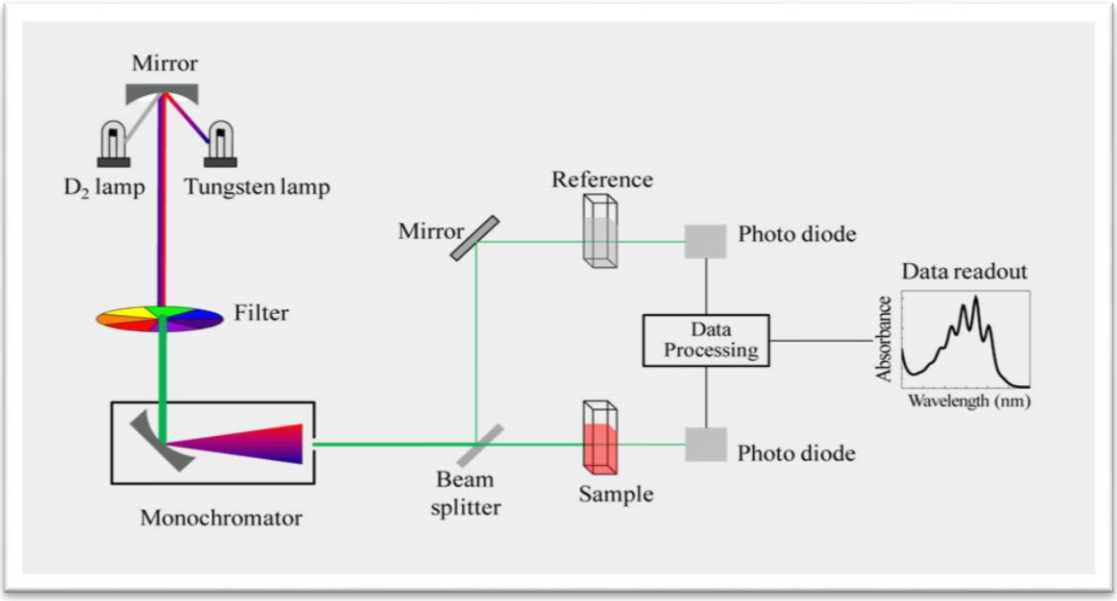

Figure (2.10) UV – Visible Spectrophotometer [85]

2-8 Crystal defects

A perfect crystal with every atom in the right place doesn't exist. Crystals usually have point defects at a single lattice point, line flaws along a row of atoms, and plane defects throughout a two-dimensional surface. Void faults are also possible [85].

Defective crystals: Flaws: Any variation from a crystal's flawless atomic arrangement causes flaws. A crystalline defect is a lattice imperfection with atomic-scale dimensions [86].

Crystalline faults fall into 4 kinds [87].

1. Zero-dimensional: Lattice-point defects
2. One-dimensional: Linear atom defects (dislocations(
3. Two-dimensional: Crystal surface planar faults
4. Volume (bulk) (void) deficiencies

Many imperfections alter solids' electrical and mechanical characteristics, and many defects are responsible for beneficial properties. Defects may seem undesirable, but they are vital to the behavior of materials. Almost all material technology relies on flaws [88].

Adding alloying elements to a metal can cause crystal defects. Imperfections in crystals affect several attributes such as strength, electrical conductivity, and ferromagnetism hysteresis loss. Thus, defects and host crystals regulate several crucial crystal properties[88].

1. Some semiconductors' conductivity is attributable to a trace amount of chemical contaminants.
2. Many crystals' colour and brilliance come from impurities.
3. Impurities can speed up atomic diffusion.
4. Imperfections usually control mechanical and plastic properties.

2.8.1 Crystal Defects Classification

The four forms of crystal defects are [89]:

1. Point defects are missing or misplaced atoms in the lattice. contain (Vacancy, Schottky, Self-interstitial, Frenkel, colour centers, polarons, excitons).
2. Atoms in linear faults are misplaced. Dislocations are linear flaws. Line imperfection is any variation from exactly periodic atom arrangement. Line defects are lattice distortions caused by

solidification, plastic deformation, vacancy condensation, or atomic mismatch in solid solutions. A dislocation is a line defect in the slip plane that separates the slipped and un-slipped regions. Stress moves dislocations. Dislocations control metals' strength and ductility.Two extreme dislocations are (Edge dislocations, Screw dislocations).

3. Surface defects are boundaries in crystalline solids that feature two-dimensional flaws and/or differing crystal structures and/or crystallographic orientations on either end. They refer to distortions around a few atomic-diameter-thick surface. External surfaces, grain boundaries, twin boundaries, stacking faults, phase boundaries. Meta-stable flaws, not thermodynamically stable. Line faults form a plane.

4. Volume defects Volume faults are 3-D. Pores, fissures, foreign inclusions, and phases During processing and production, these flaws occur. All these faults might raise stress, affecting the parent metal's mechanical behaviour. Foreign particles are sometimes added to reinforce the parent substance. Foreign particles act as impediments to dislocation migration, allowing plastic deformation. Second-phase particles can either be cut by dislocations or resist cutting, forcing dislocations to bypass them. Ordered particles give many superalloys high-temperature strength. Porosity reduces load-bearing area and increases stress..

Chapter Three

Experimental Work

3.1 Introduction

This chapter focuses on the details of the experiments used to make iron oxide nanofilms using the thermal evaporation method. Thin films were made and tested by X-ray diffraction (XRD), scanning electron microscopy (SEM), and atomic force microscopy (AFM). Also look into the spectroscopy of the optical properties. Figure (3.1) shows a diagram of the experimental work, from the materials to the characterization of the films.

3.2 Material Used:

Iron powder (Fe): It was observed as powder from 3302 Twig Leaf Ln, Houston, TX 77084, USA, with grain size 1 μm and high purity (99 %).

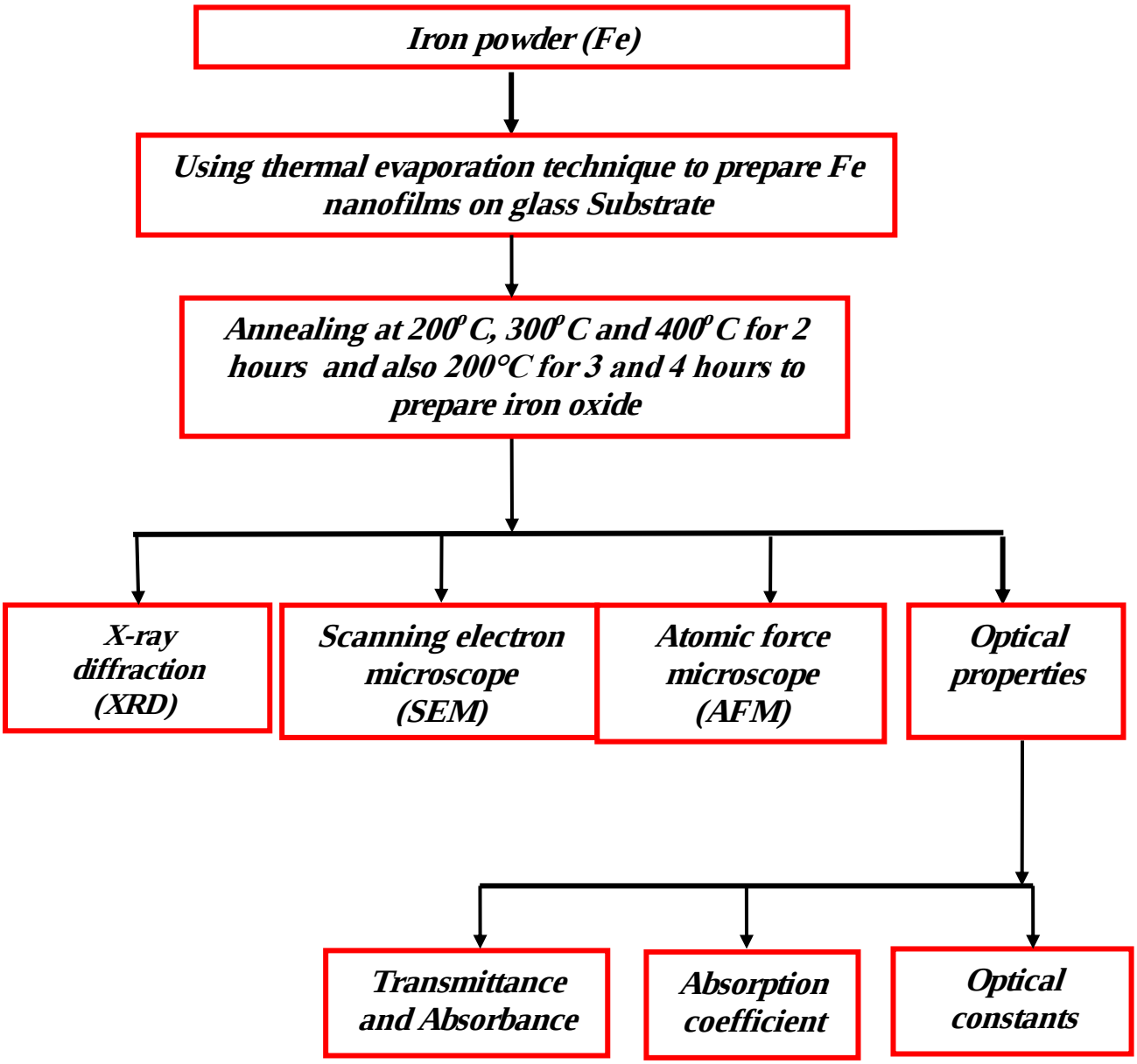

Fig.(3.1) Experimental work shown as a diagram

3.3 Substrate Preparation

As substrates, 0.1–0.12 cm thick glass slides with a (2×2) cm^2 area were used. The following things were done to these glass slides:

1. Alcohol was used to clean the substrates.
2. The substrates were put in a clean beaker with distilled water and then washed for 10 minutes with an ultrasonic cleaner.
3. The glass substrates were then dried with an air jet and smoothed with soft paper.

3.4 Evaporation Boat

The most commonly used materials for evaporation boat are metals with a high melting point, such as tungsten (W) (M.P = 3370 ^oC), and molybdenum (Mo) (M.P = 2622 ^oC). In this work, one type of boat were used for the evaporation which is molybdenum boat for the deposition of Fe nanofilms, as shown in figure (3.2).

Fig.(3.2) Molybdenum boat .

3.5 The Coating Unit

The vacuum unit system is:

1 Edwards Auto 306.
2 Heats evaporates using tungsten or molybdenum filaments.
3 $1x10^{-7}$mbar maximum chamber pressure.
4 Typical filament currents are 100-200 A.
5 Exposes substrate to visible or IR radiation.
6 1.5 μm maximum deposition thickness

The main constructions of the typical vacuum coating unit are shown in figure (3.3).

Fig.(3.3) Thermal evaporation system.

3.6 Thin Film Growth

The deposition of Fe nanofilms have been performed by electrical resistance heated thermal evaporation process. Electrical power is delivered through the boat to create a vapour that passes right to the substrate. Any vacuum deposition technique has three steps: creating an evaporant from the source material, transporting the evaporant to the substrate, and condensing the evaporant on the substrate to produce the thin film as shown in figure (3.4). This work uses room-temperature evaporation (RT). The evaporation rate was 0.8 $nm.s^{-1}$ at 10^{-6} mbar. 15 cm separated source and substrate.

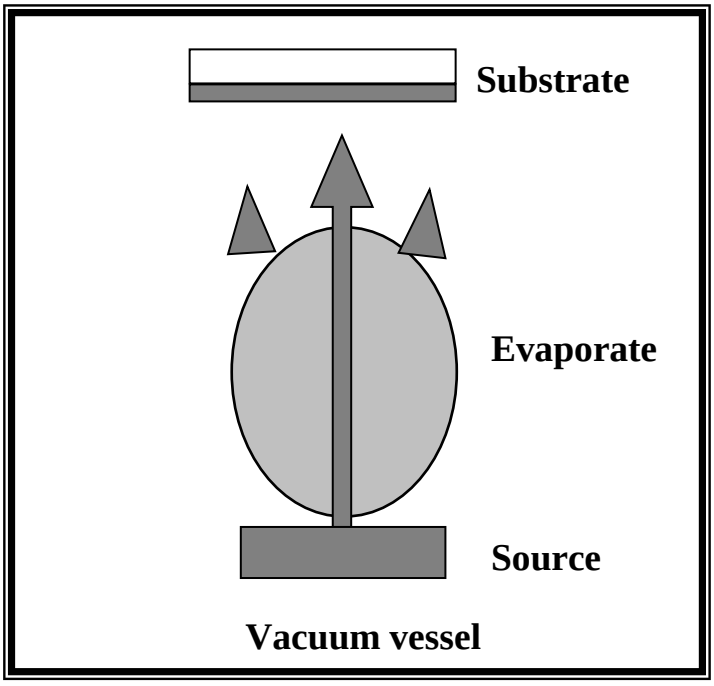

Fig.(3.4) Basic steps deposition processes.

3.7 Thickness Measurement

One of the most important things about a thin film is how thick it is. There are several ways to figure out how thick a thin film is. Optical measurement and the weight method were used to figure out how thick the films were.

3.8.1 Optical measurement method

Optical interferometry measures film thickness. This approach uses laser beam interference from thin film surface and substrate bottom. The thickness was estimated by the difference in optical path lengths of the two reflections using a He-Ne laser (632 nm) as shown in figure (3.5).

Fig.(3.5) Optical thin film measurement.

3.8.2 The weight method

Thickness of the thin films has been calculated according to the following equation [90]:

$$t = \frac{m}{2\pi\rho R^2} \quad \text{……..…..} \quad (3\text{-}1)$$

where t is film thickness (nm), m is material mass (g), is material density (g/cm^3), and R is substrate-to-boat distance (cm).

This method gives an approximate thickness because not all the material is deposited on the substrate but some of the material lost or fleeing on the sides of the heater.

3.9 Structural and Morphological Measurements

3.9.1 X-ray diffraction (XRD)

These measurements examine the thin film structure. This experimental technique is used to identify the overall structure of bulk solids, including lattice constants, unknown material identification, single crystal orientation, polycrystal orientation, flaws, stresses, etc. X-ray diffraction using SHIMADZU XRD-6000, which measures intensity based on Bragg's angle. System conditions:

Source Cu Kα emits electromagnetic radiation with a wavelength of 1.5406 Å. The target value for the Cu Current is 30 mA.Voltage = 40 kV. Scanning speed is equal to 0.25 degrees per minute, and X-ray examinations are carried out at angles ranging from 0 degrees to 80 degrees, as illustrated in the figure (3.6).

Fig.(3.6) System of the XRD.

3.9.2 Scanning Electron Microscopy (SEM)

One or two condenser lenses focus scanning electron microscopy (SEM) to a 0.4- to 5-nm point. The beam passes via pairs of scanning coils or deflector targets in the electron column, often in the last lens, which deflect the beam in the x and y axes so it scans in a raster way over a rectangular sample surface (3.7).

Fig.(3.7) System of the SEM

3.9.3 Atomic Force Microscope (AFM).

Atomic force microscopes (AFM) allow molecular examination of surfaces. Instead of photos, topography data is collected. AFM measures the size and other properties of manufactured nanoparticles. Figure shows AFM operation as shown in figure (3.8). All samples are AFM nanoscope-studied.

Fig.(3.8) System of AFM.

3.9.4 Optical Measurement

The measurements of the optical components As illustrated in figure (3.9), one can generate thin films by employing a spectrophotometer with a wavelength range of 200 to 1100 nm, which was manufactured by the Japanese company Phillips and sold under the brand name Shimadzu UV-1650 PC. These optical measurements are used as a basis for the calculation of the optical characteristics.

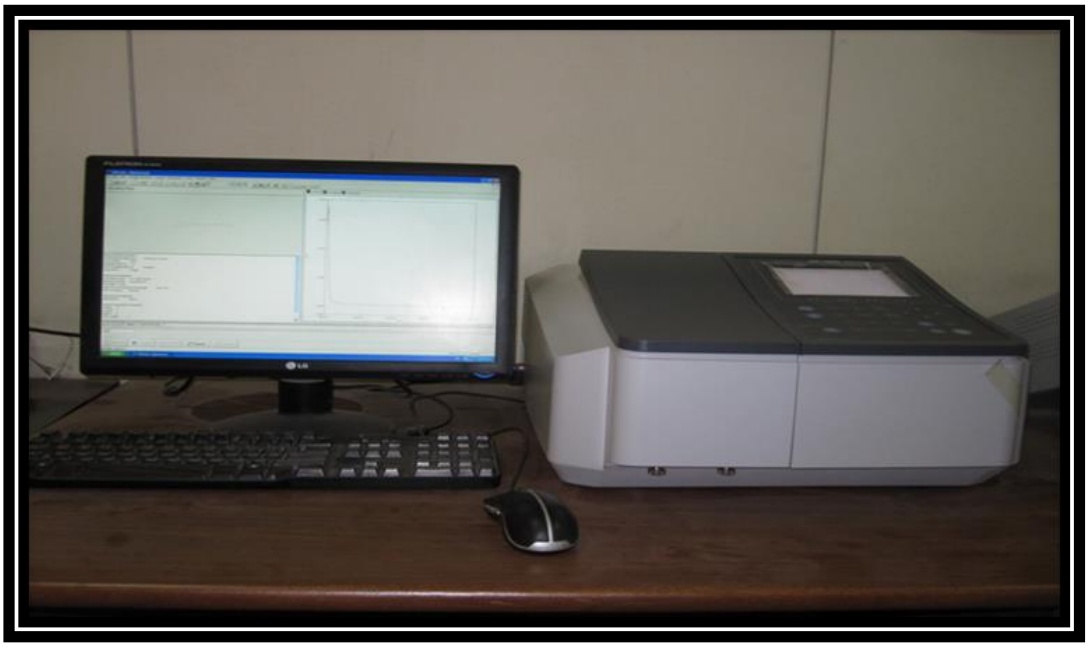

Fig.(3.9) Photographic of UV-VIS-NIR spectrophotometer.

Chapter Four

Results and Discussion

4.1 Introduction

This chapter presents the results and discussion of the structural, morphological and optical properties of pure Fe nanofilms with different annealing temperature. These are deposited on glass substrates by thermal evaporation technique.

4.2 Structural and Morphological Properties

4.2.1 X-ray Diffraction of different annealing temperature Fe

Figure (4.1) shows the X-ray diffraction pattern of pure iron nano films deposited on glass substrates by thermal evaporation technique, where the thickness of the film was 75 nm. The prepared nanofilms subjected to different annealing temperature of 200^{o}C, 300^{o}C and 400^{o}C for 2 hours as shown in figures (4.2-4.4) , also the nanofilms subjected to annealing temperature at 200°C for 3 and 4 hours as in Figures 4.5 and 4.6. Peaks of XRD were recorded between 10^{o}-80^{o}.
Figure (4.1) display three salient diffraction peaks at 2θ = 41.365^{o}, 48.156^{o} and 64.432^{o} corresponding to miller indices (100), (101) and (102) for crystalline hexagonal structure of Fe taken from the card file data (34-0529). Figure (4.2) display three salient diffraction peaks at 2θ = 15.577^{o}, 26.288^{o} and 24.378^{o} corresponding to miller indices (103), (116) for crystalline tetragonal structure γ-Fe_2O_3 (maghemite) taken from the card file data (25-1402) and (012)* for crystalline hexagonal crystal structure α-Fe_2O_3 (hematite) taken from the card file data (33-0664) respectively. Figure (4.3) display four salient diffraction peaks at 2θ = 16.200^{o} , 26.288^{o}, 30.85^{0}, and 24.135^{o} corresponding to miller indices (103),(116) and (206) for crystalline tetragonal structure γ-Fe_2O_3 taken from the card file data (25-1402) , and (012)* for crystalline hexagonal structure α-Fe_2O_3 taken from the card file data (33-0664) respectively.

Figure (4.4) display three salient diffraction peaks at 2θ = 26.288^{o}, 31.198^{o}, and 41.365^{o} corresponding to millers indices (206) and (116) for tetragonal crystal structure γ-Fe_2O_3 taken from the card file data (25-1402) , and (113)* for hexagonal crystal structure α-Fe_2O_3 taken from the card file data (33-0664) respectively .

Figure (4.5) display five salient diffraction peaks at 2θ = 14.084^{o} , 26.288^{o} , 24.2 , 54.123^{o} and 70.014^{o} corresponding to miller indices (103) and (116) for crystalline tetragonal structure γ-Fe_2O_3 taken from the card file data (25-1402) and (206), (116)* and (208)* for hexagonal crystal structure α-Fe_2O_3 taken from the card file data (33-0664) respectively. Figure (4.6) display two salient diffraction peaks at 2θ = 30.838^{o}, and 32.176^{o} corresponding to millers indices (206) and (216) for tetragonal crystal structure γ-Fe_2O_3 taken from the card file data (25-1402). Annealing at different temperature and time in the presence of air leads to oxidation and reveal the mixed phases of iron oxide maghemite and hematite , implying that annealing played a role of a surfactant to some extent and contributed to the increase in crystallization, and here we must point out that the oxidation at 200^{o}C for 4 hours leads to growth of maghemite phase only.

The average crystallite size of samples annealed at different temperature and time was estimated from the peak broadening of diffraction pattern using Scherrer's formula (Equation 2-2) , due to finite size of crystallites. From these figures it can be seen that the average crystallite size increased with increasing annealing temperature and time as can be seen in the Table (4.1).

The intensity of peaks increasing with decreased annealing time which attributed to increase in crystallite size, which mean enhancement of degree of crystallite. Similar behaviour was reported in the researcher [35].

The change in the values of micro strain (*S*),dislocation density(δ), number of crystals per area (N), and number of layers (N_t) were calculation from Equations { (2-3), (2-4), (2-5) and (2-6) Respectively } of nanofilms follow the change that has accompanied the crystallite size which is listed in Table (4.2) . It has been found that when increase the annealing temperature or time the micro strain decreases and the crystallite size increase, because there is no delay in crystal growth which is due to the pressures that can decrease the lattice energy and increase the driving force to growth [91].

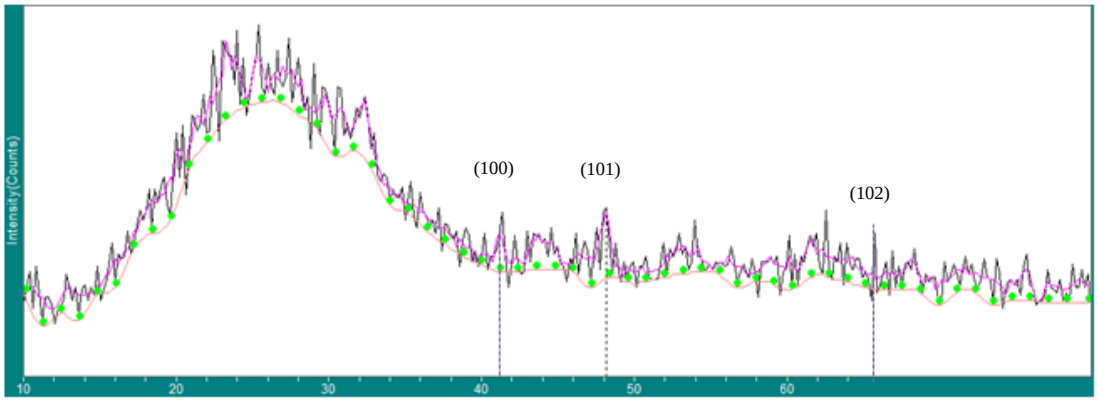

Fig.(4.1): XRD spectrum of as-deposited Fe nanofilm

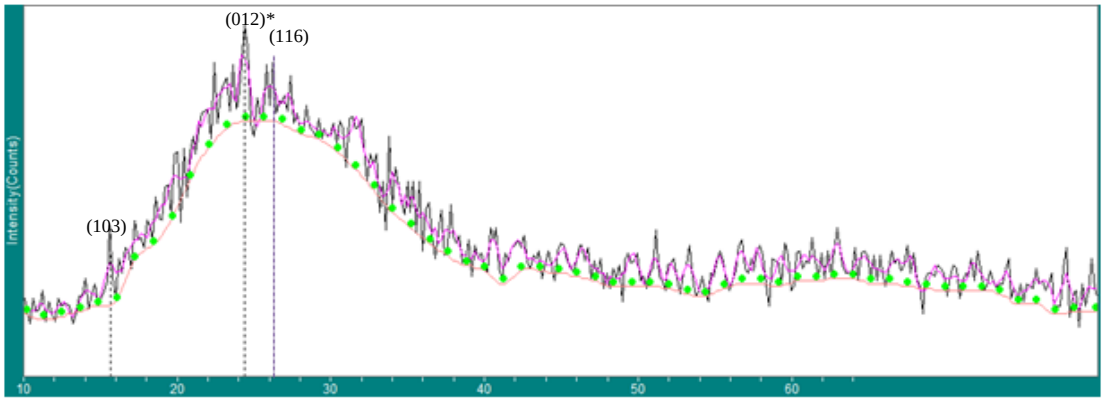

Fig.(4.2): XRD spectrum of iron oxide nanofilm annealed at 200^{o}C for 2 hours

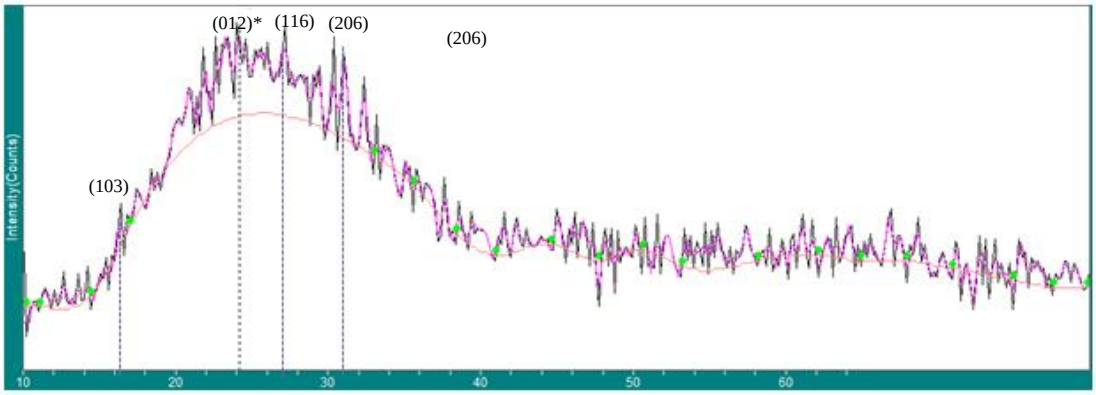

Fig.(4.3): XRD spectrum of iron oxide nanofilm annealed at 300^{o}C for 2 hours

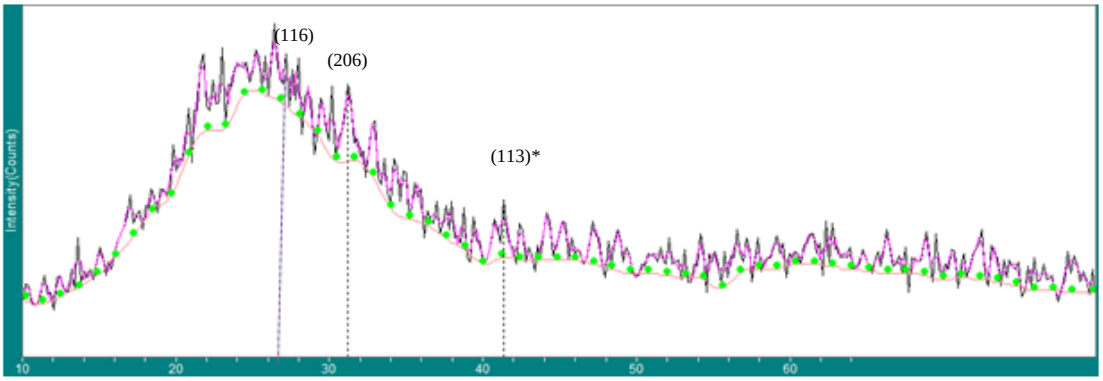

Fig.(4.4) XRD spectrum of iron oxide nanofilm annealed at 400^{o}C for 2 hours

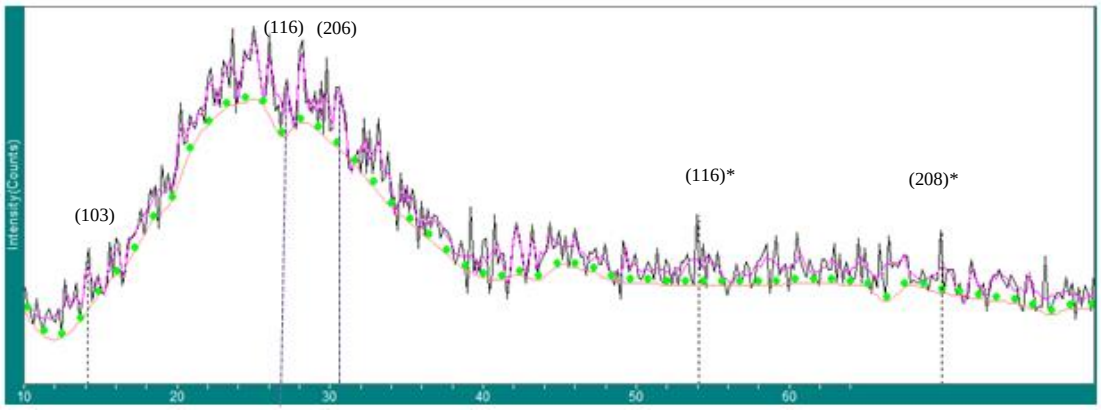

Fig.(4.5): XRD spectrum of iron oxide nanofilm annealed at 200^{o}C for 3 hours

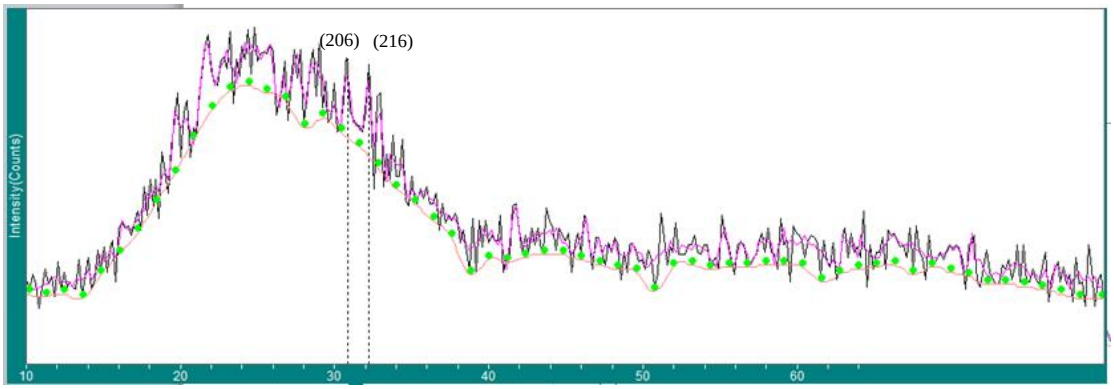

Fig.(4.6): XRD spectrum of iron oxide nanofilm annealed at 200°C for 4 hours

Table (4-1): Obtained result from the XRD for prepared nanofilms

Annealing with time (hour)	2θ Degree	(hkl)	FWHM (degree)	a (A^0)	b (A^0)	c (A^0)	d (Å)	Crystallite size (nm)	Average crystallite size (nm)
As-deposited	41.765	(100)	0.439	2.45	2.45	3.93	2.12	18.12	15.12
	48.156	(101)	0.783	2.45	2.45	3.93	1.84	11	
	64.432	(102)	0.489	2.45	2.45	3.93	1.44	16.24	
200°C for 2 hours	15.577	(103)	0.351	8.34	8.34	25.02	0.568	22.84	18.06
	24.378	(012)*	0.568	5.035	5.035	13.74	0.364	14.31	
	26.288	(116)	0.466	8.34	8.34	25.02	3.400	17.04	
300°C for 2 hours	16.200	(103)	0.351	8.34	8.34	25.02	0.568	22.84	18.28
	24.135	(012)*	0.522	5.035	5.035	13.74	0.364	15.56	
	26.288	(116)	0.466	8.34	8.34	25.02	3.400	17.04	
	30.85	(206)	0.466	8.34	8.34	25.02	0.286	17.68	
400°C for 2 hours	26.288	(116)	0.466	8.34	8.34	25.02	3.400	17.04	18.43
	31.198	(206)	0.436	8.34	8.34	25.02	0.286	18.91	
	41.365	(113)*	0.439	5.035	5.035	13.74	3.93	19.34	
200°C for 3 hours	14.084	(103)	0.347	8.34	8.34	25.02	0.628	23.07	19.02
	26.288	(116)	0.466	8.34	8.34	25.02	3.400	17.04	
	30.838	(206)	0.466	8.34	8.34	25.02	0.286	17.68	
	54.123	(116)*	0.51	5.035	5.035	13.74	0.169	17.49	
	70.014	(208)*	0.489	5.035	5.035	13.74	0.134	19.83	
200°C for 4 hours	30.838	(206)	0.466	8.34	8.34	25.02	0.286	17.68	21.67
	32.176	(216)	0.322	8.34	8.34	25.02	0.277	25.67	

(∗)α-Fe_2O_3 (hematite phase) , and the others γ-Fe_2O_3(maghemite phase)

Table (4-2): Number of crystals per area (N) and dislocation ($\mathcal{Z}$).

Annealing with time (hour)	Number of crystals per area (N)$(nm)^{-2}$	Dislocation (δ) (Line/nm^2)	Number of layers (N_t)	micro strain (S)
As-deposited	0.021697	0.004374	4.960317	0.002237
200°C for 2 hours	0.021697	0.004374	4.960317	0.001972
300°C for 2 hours	0.012732	0.003066	4.152824	0.00192
400°C for 2 hours	0.012278	0.002993	4.102845	0.001867
200°C for 3 hours	0.011981	0.002944	4.069452	0.001834
200°C for 4 hours	0.0109	0.002764	3.943218	0.001654

4.2 Atomic Force Microscope (AFM)

The typical AFM scans of the prepared iron oxide nanofilms as deposited and different annealing with time at (200 °C, 300 °C, 400 °C) for 2 hours, and 200 °C for 3and 4 hours are presented in figures (4.7-4.12) respectively. From each figures, contain images 3D, Histogram grain and Height distribution. The AFM images of iron oxide nanofilms show a high surface homogeneity in which the distribution of crystalline granules is uniform which is evident from the convergence of the roughness and root mean square (RMS) values as in Table (4-3). The white areas of the images indicate that there are set of crystalline granules one on top other, so it can be believe that the adjacent granules come together to form large clusters; therefore, we find that the granules in the white areas are larger than that in other regions. The roughness and root mean square (RMS) values are increased from 1.1 nm and 1.43 nm as-deposited nanofilm to 8.35 nm and 10.6 nm annealed at 200 °C for 4 hours, which is attributed to the fact that the surface diffusion was sufficient due to the deposition temperature. The increase in RMS lead to increase in crystalline growth in vertical direction more than horizontal direction. Also Table (4.3) contain the ten point height and the average

diameter. The values of ten point height confirm the roughness and RMS results. Similar behaviour was reported in [92].

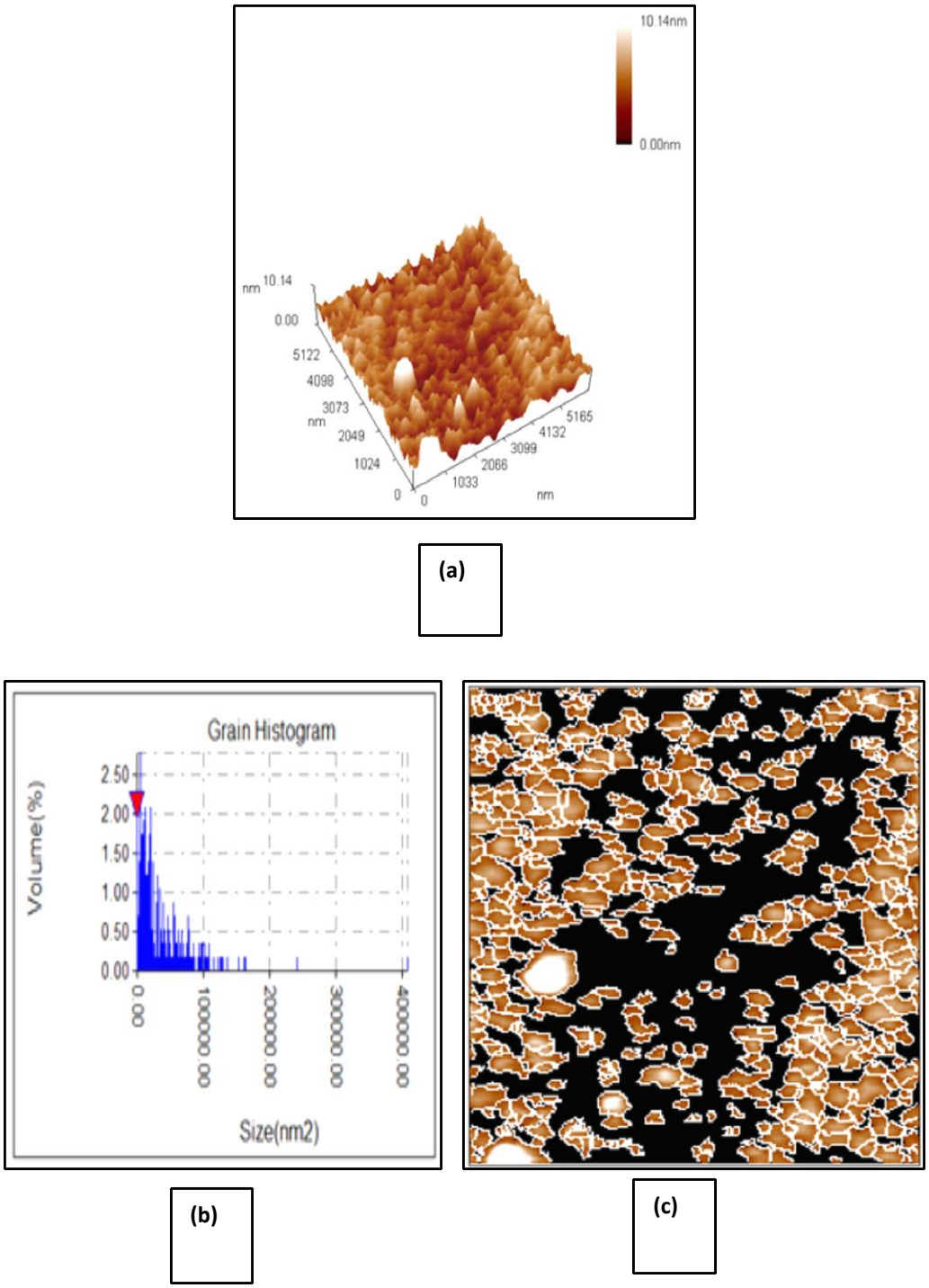

Fig.(4.7): AFM images of iron oxide nanofilms as-deposited for a)3D, b) Histogram grain and c) Height distribution with data report

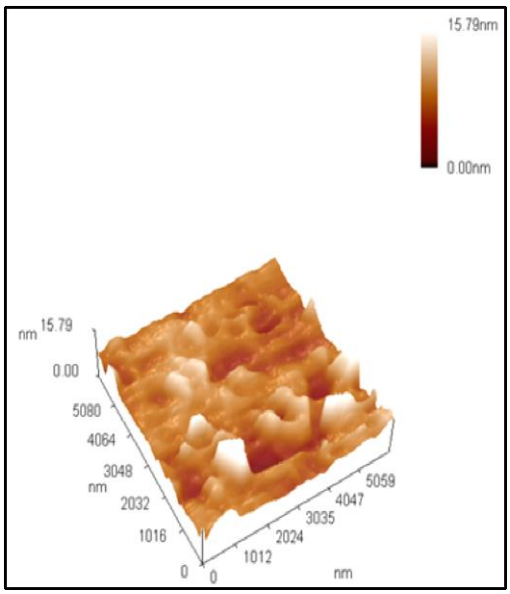

(a)

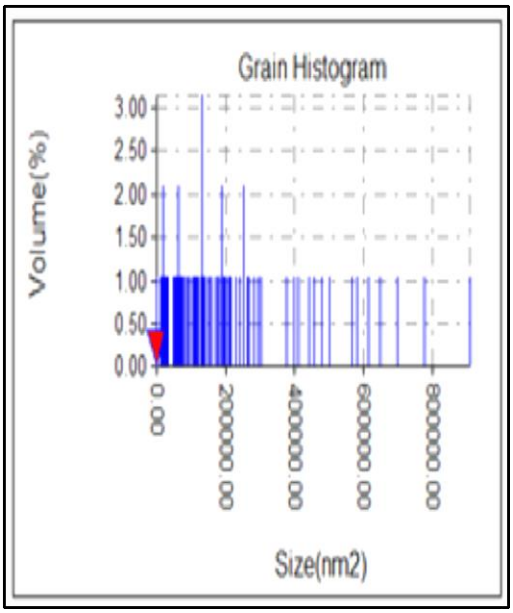

(b)

(c)

Fig.(4.8): AFM images of iron oxide nanofilms annealing at 200°C for 2h for a) 3D, b) Histogram grain and c) Height distribution with data report

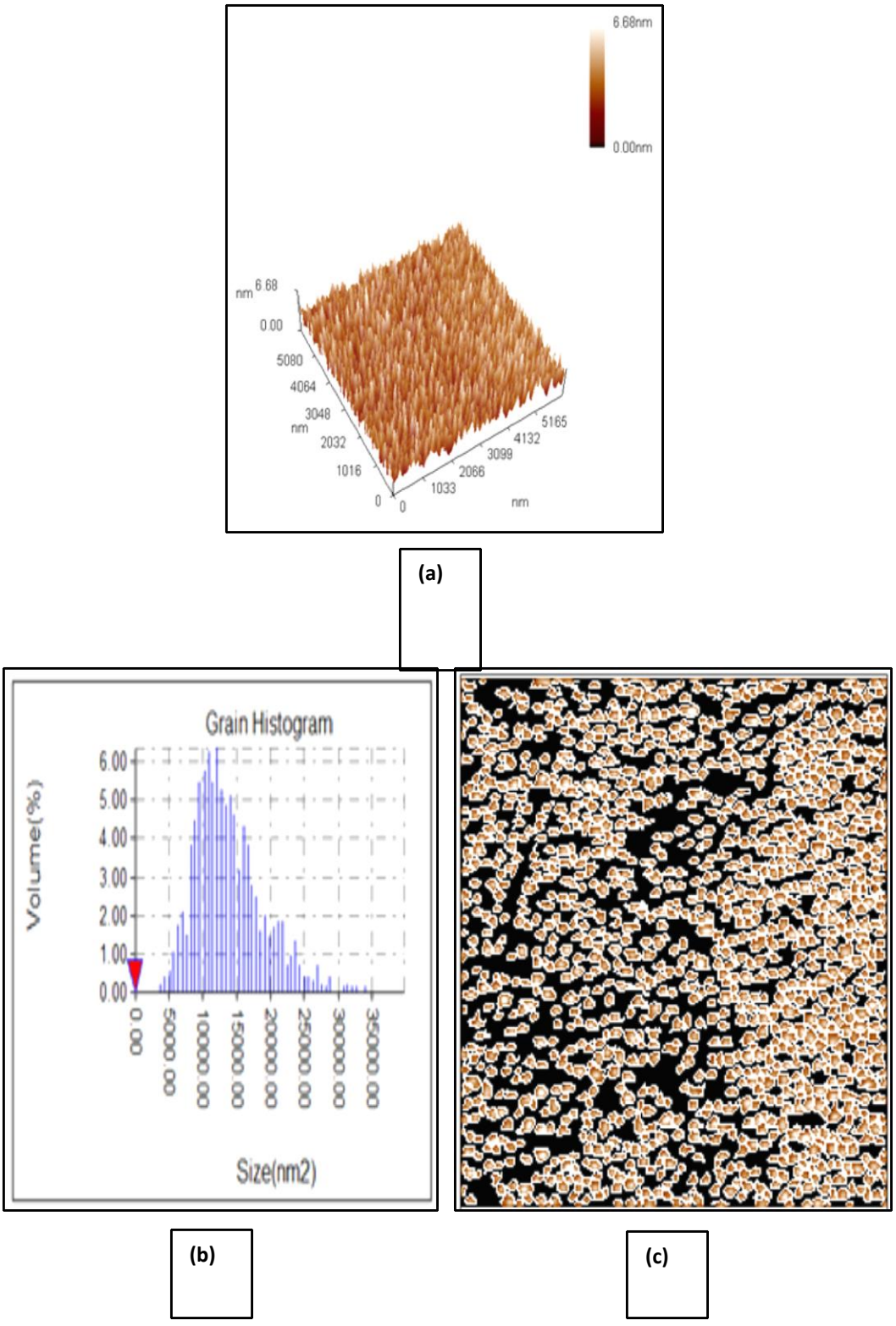

Fig.(4.9): AFM images of iron oxide nanofilms annealing at 300°C for 2h for a) 3D, b) Histogram grain and c) Height distribution with data report

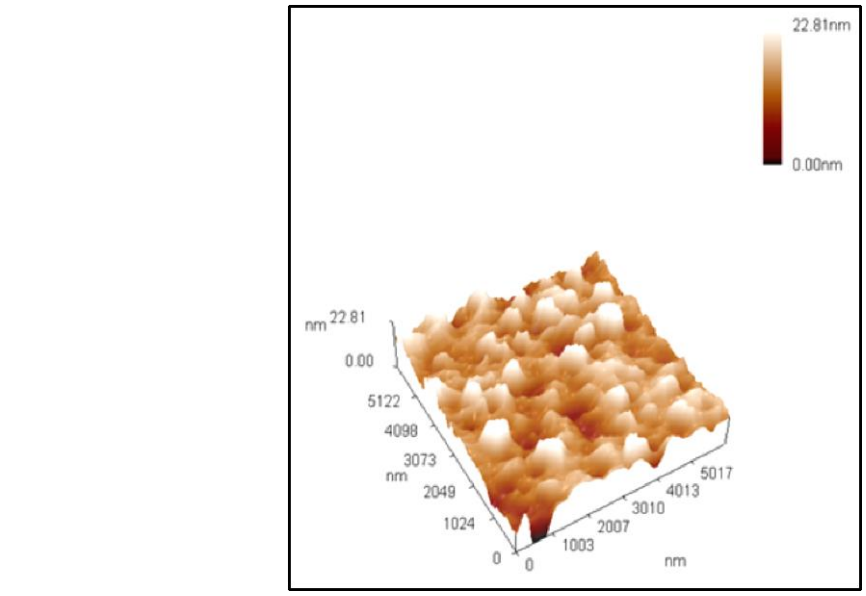

(a)

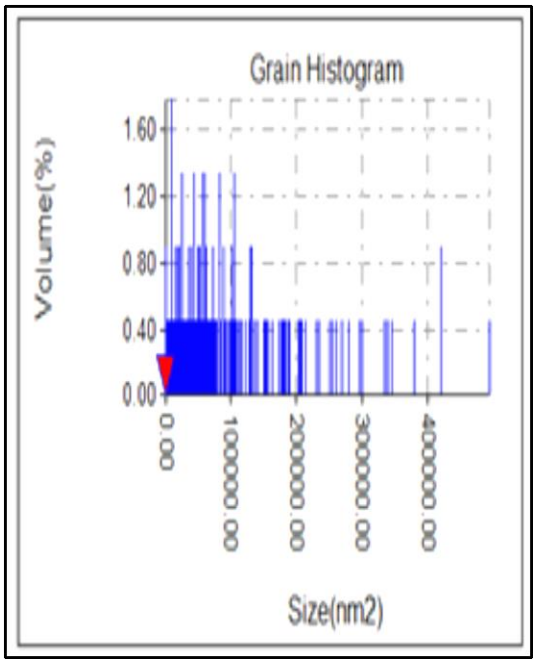

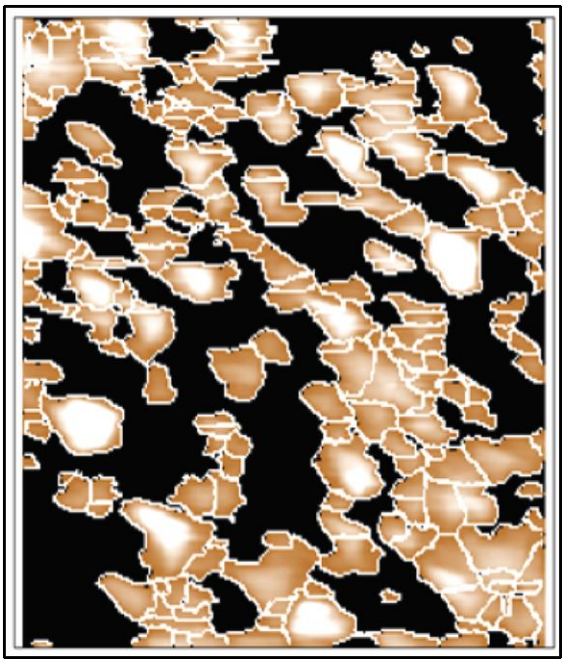

(b)

(a)

(c)

Fig.(4.10): AFM images of iron oxide nanofilms annealing at 400^{o}C for 2h for a) 3D, b) Histogram grain and c) Height distribution with data report.

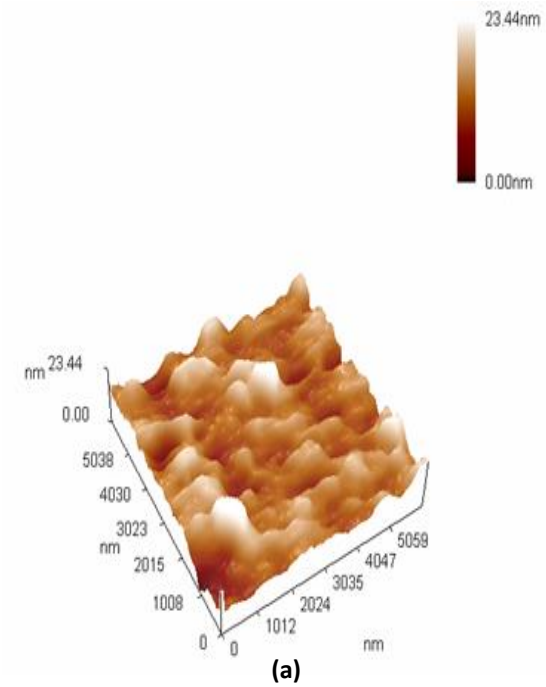

(a)

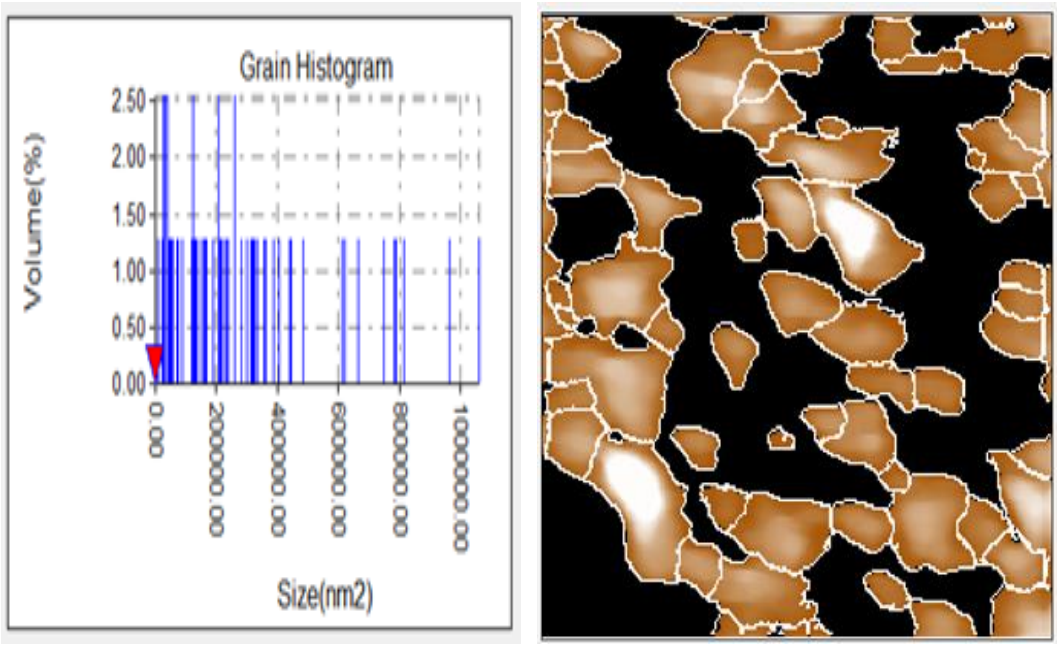

(b) (c)

Fig.(4.11): AFM images of iron oxide nanofilms annealing at 200°C for 3h for a) 3D, b) Histogram grain and c) Height distribution with data report

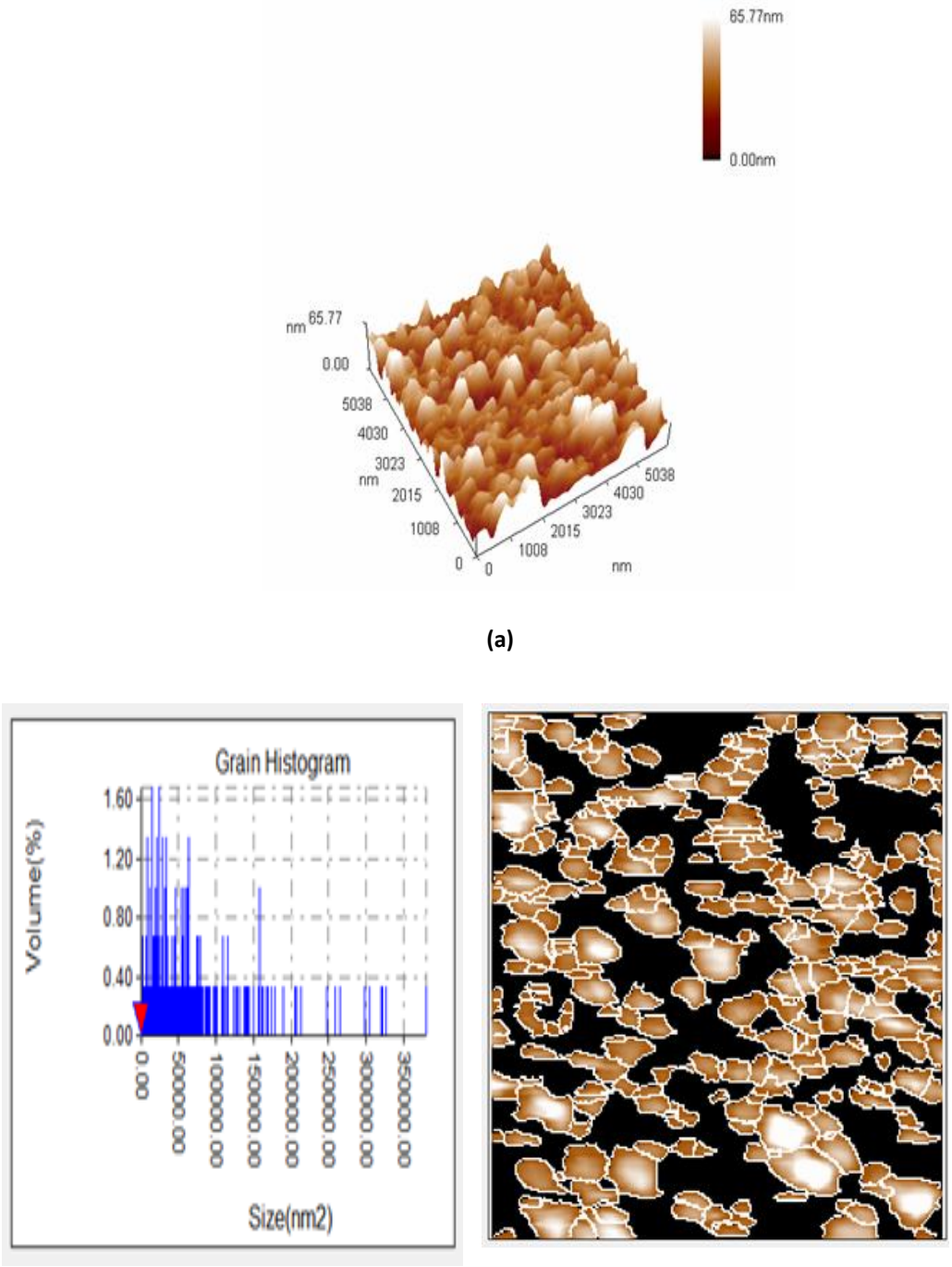

Fig.(4.12): AFM images of iron oxide nanofilms annealing at 200^{o}C for 4h for a) 3D, b) Histogram grain and c) Height distribution with data report

Table (4.3): AFM of iron oxide with different annealing with time

Annealing with time (h)	Roughness average (nm)	Root mean square (nm)	Ten point height (nm)	Average Diameter(nm)
as-deposited	1.1	1.43	8.74	201.9
200°C for 2h	1.33	1.91	10.1	499
300°C for 2h	0.806	1.01	6.64	133.9
400°C for 2h	2.61	3.4	18.2	323.1
200°C for 3h	2.49	3.25	14.5	542.4
200°C for 4h	8.35	10.6	63.2	276.7

4.3 - Scanning Electron Microscope (SEM)

The typical SEM micrographs of the prepared iron nanofilm as deposited and different annealing temperatures at 200 ^{o}C, 300 ^{o}C, and 400 ^{o}C for 2 hours, and also different annealing times at 200 ^{o}C for 3 and 4 hours are presented in Figures (4.13-4.18) respectively. Annealing at different temperatures and times contributed to increase of the average particle sizes. As shown in such figures and Table 4.1, the values of the average particle size of the oxidation mixed phases of iron oxide hematite α-Fe_2O_3 and maghemite γ-Fe_2O_3 nanoparticles deduced from SEM micrographs and their corresponding XRD agree reasonably well, thus indicating a high degree of crystallinity.

Some special particle shapes can be noted depending on the annealing temperatures and annealing times, the iron that is prepared as-deposited appears as a spherical shape as in figure (4.13), while the films that are annealed at 200 ^{o}C for 2 and 3 hours showed that the assemblies of nanoparticles in the form of a flowers-like shape of Fe_2O_3 spread on the film surface appears as a flower-like shape of Fe_2O_3 spread on the film surface as in figure (4.13 and 4.17). Thus these films are candidates for

energy storage applications. Figures (4.15 and 4.16) show the needle-like particles of Fe_2O_3 for the films that were annealed at 300 ºC and 400 ºC for 2 hours respectively. Figure (4.18) shows the agglomerate spherical particles and layers that are candidates for energy storage applications.

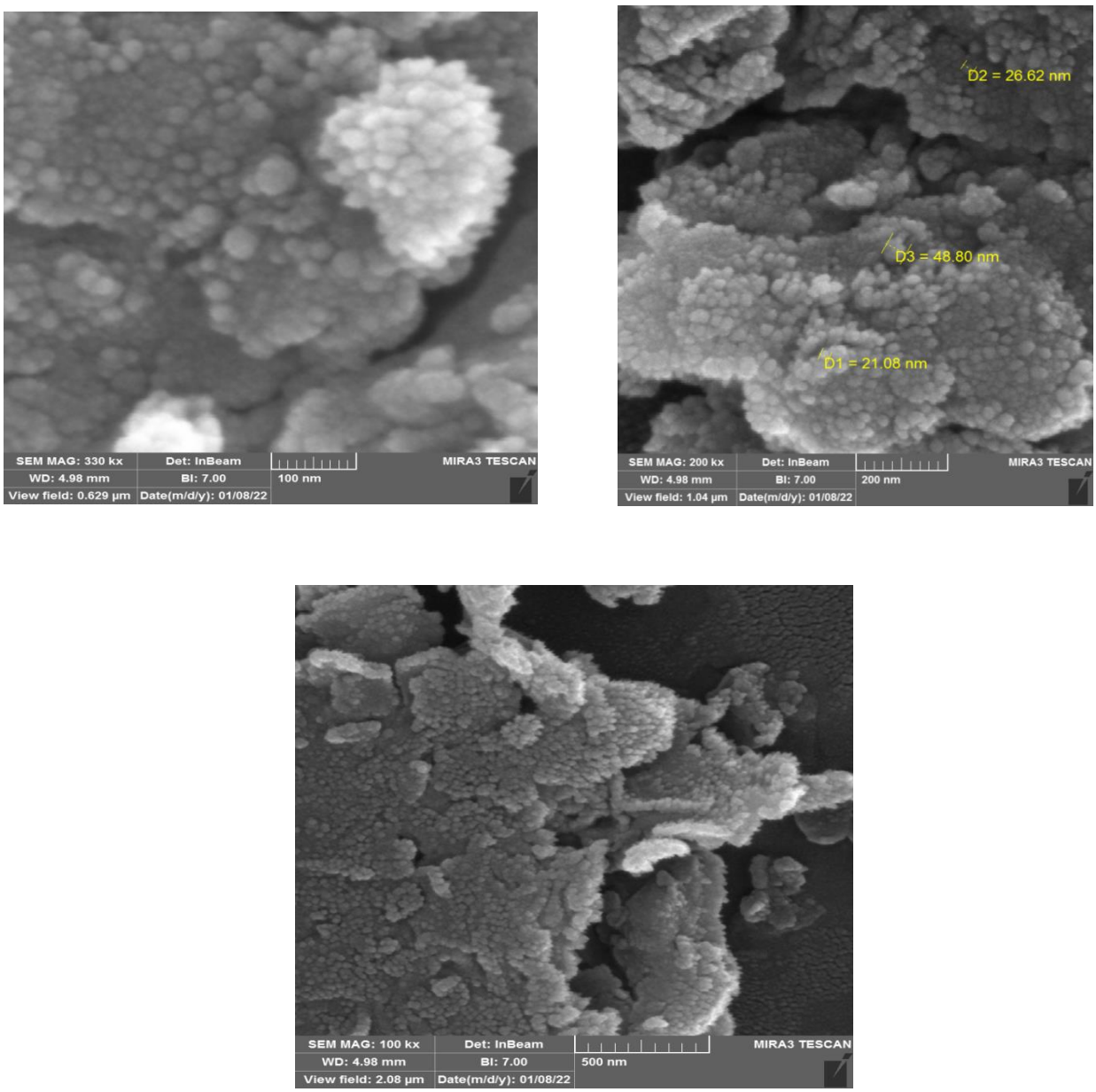

Fig.4.13: SEM of as deposited iron nanofilm at different magnification

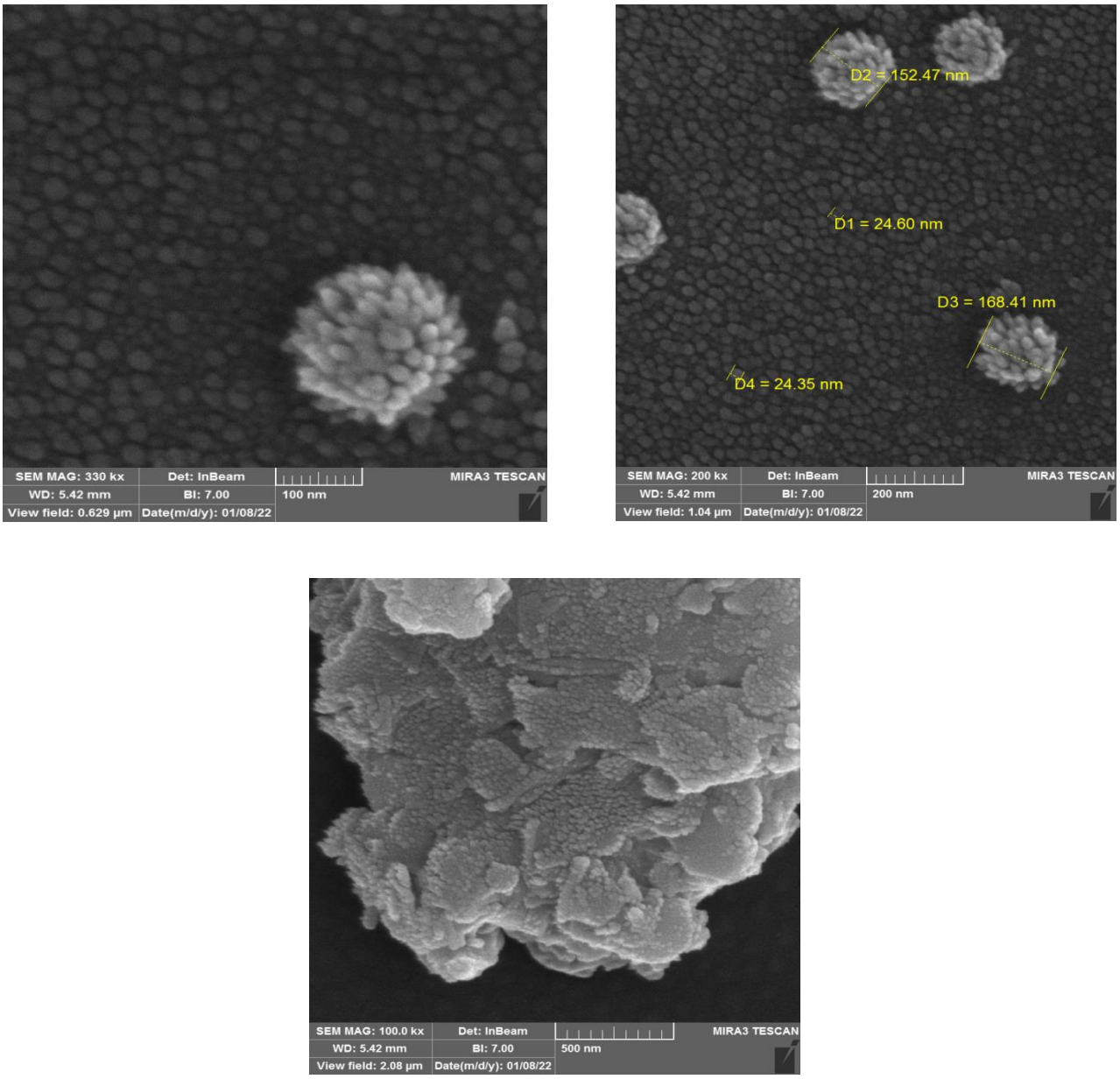

Fig.4.14: SEM of iron oxide nanofilm annealed at 200^{o}C for 2 hours at different magnification

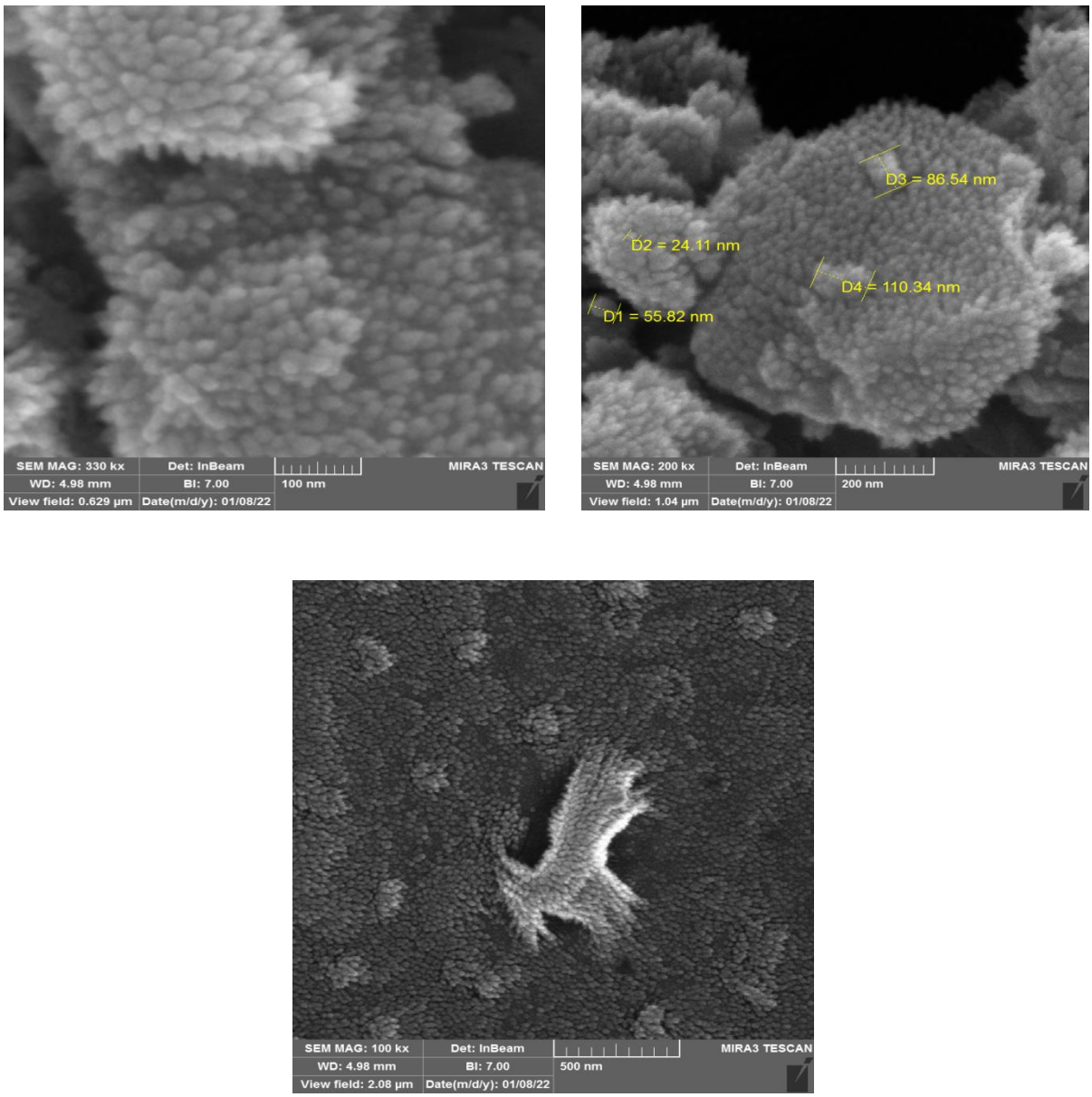

Fig.4.15: SEM of iron oxide nanofilm annealed at 300^{o}C for 2 hours at different magnification

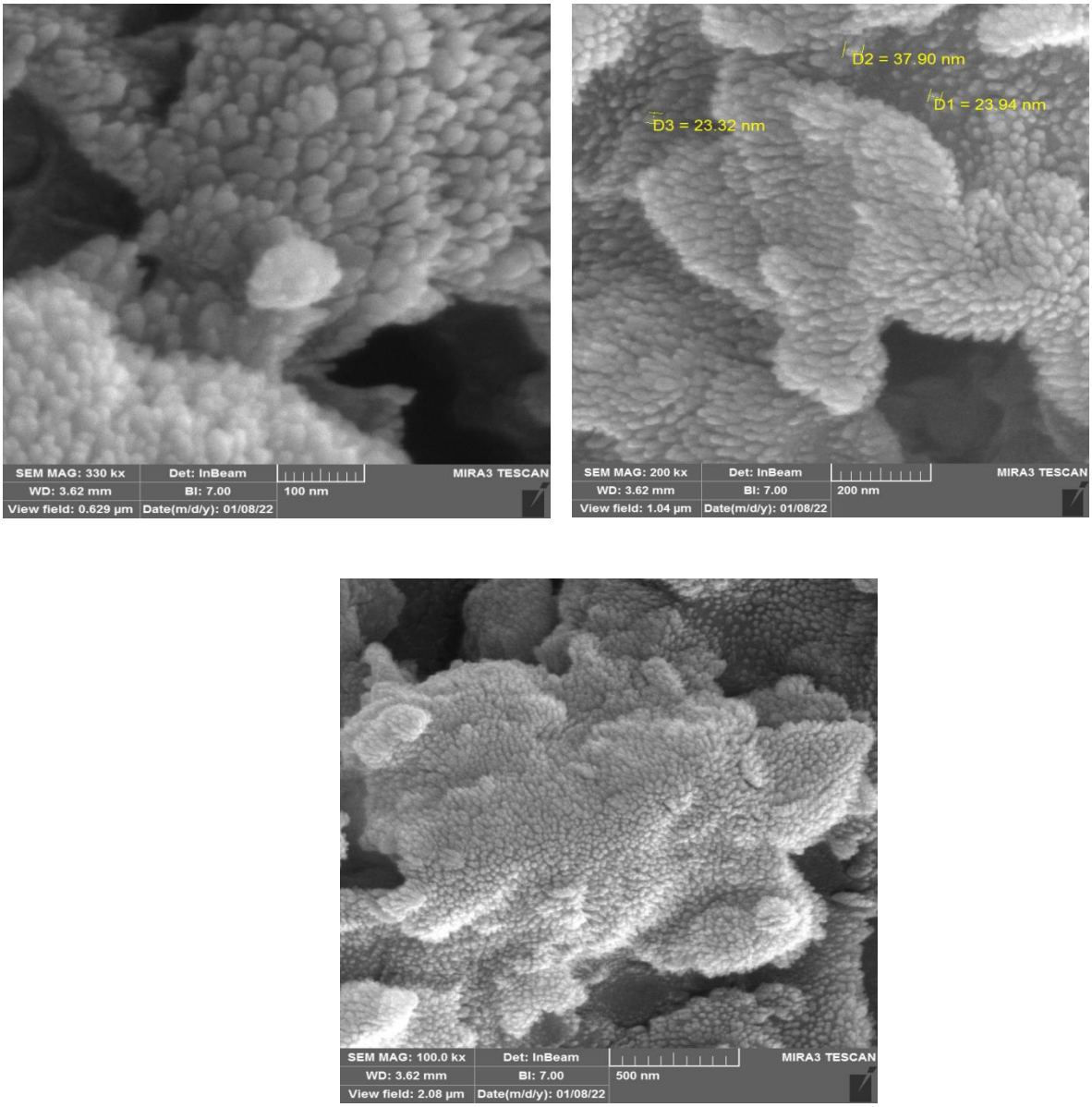

Fig.4.16: SEM of iron oxide nanofilm annealed at 400^{o}C for 2 hours at different magnification

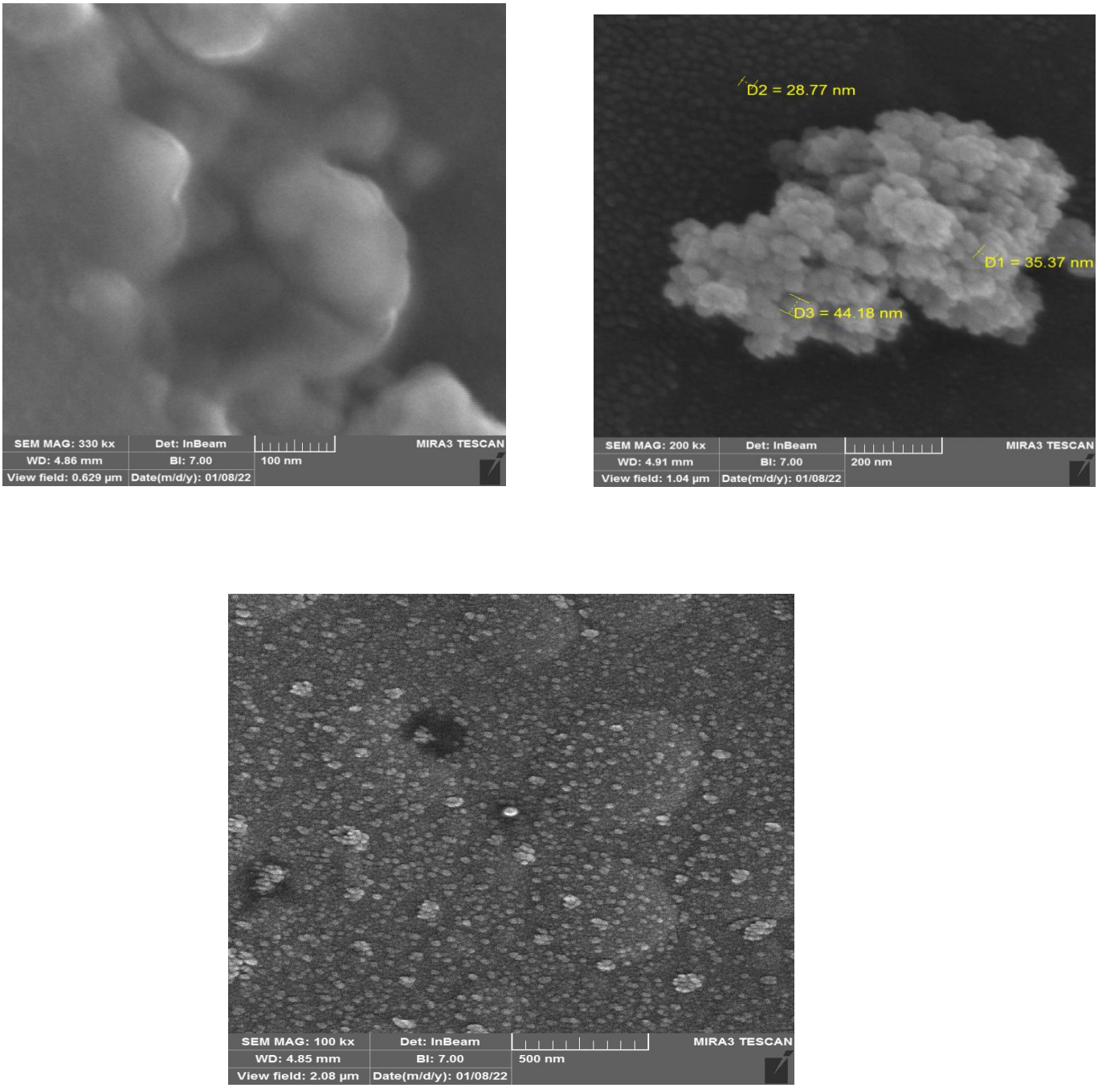

Fig.4.17: SEM of iron oxide nanofilm annealed at 200^{o}C for 3 hours at different magnification

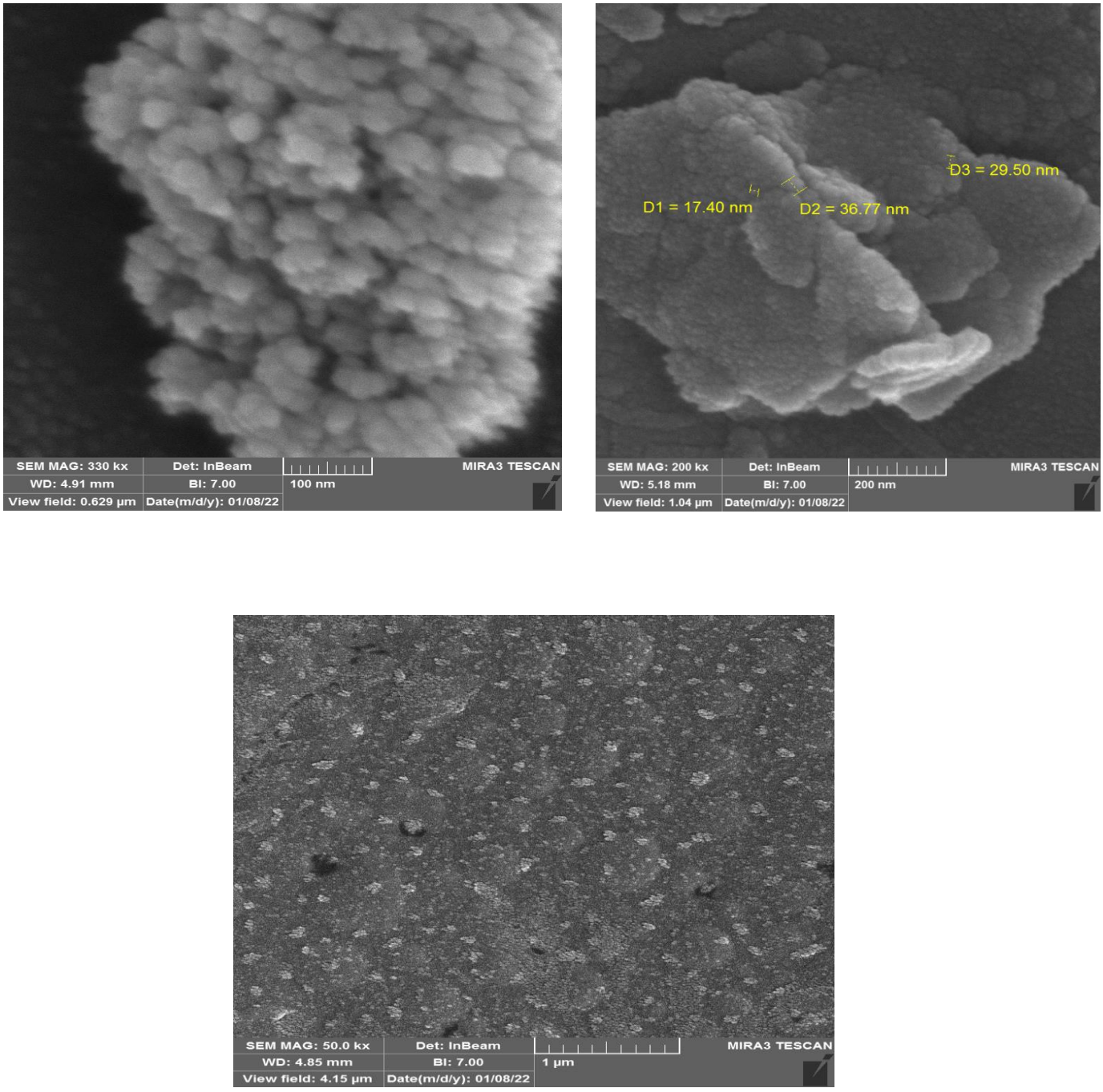

Fig.(4.18): SEM of iron oxide nanofilm annealed at 200^{o}C for 4 hours at different magnification

4.4 Optical properties

4.4.1 Absorbance (A)

The absorbance spectra of Fe nanofilm as-deposited and different annealed temperature 200 ^{o}C , 300 ^{o}C and 400 ^{o}C for 2 hours as a function of wavelength are shown in figure (4.19) and different annealed time three and four hours for 200^{o}C as a function of wavelength are shown in figure (4.20). From the figure (4.19), it was observed that the absorbance increases with increasing annealing temperature in the UV region and then decreases with increasing annealing temperature in the visible and NIR regions, while in figure (4.20), the absorbance decrease with increasing annealing time. This result is consistent with the findings of the researchers [93].

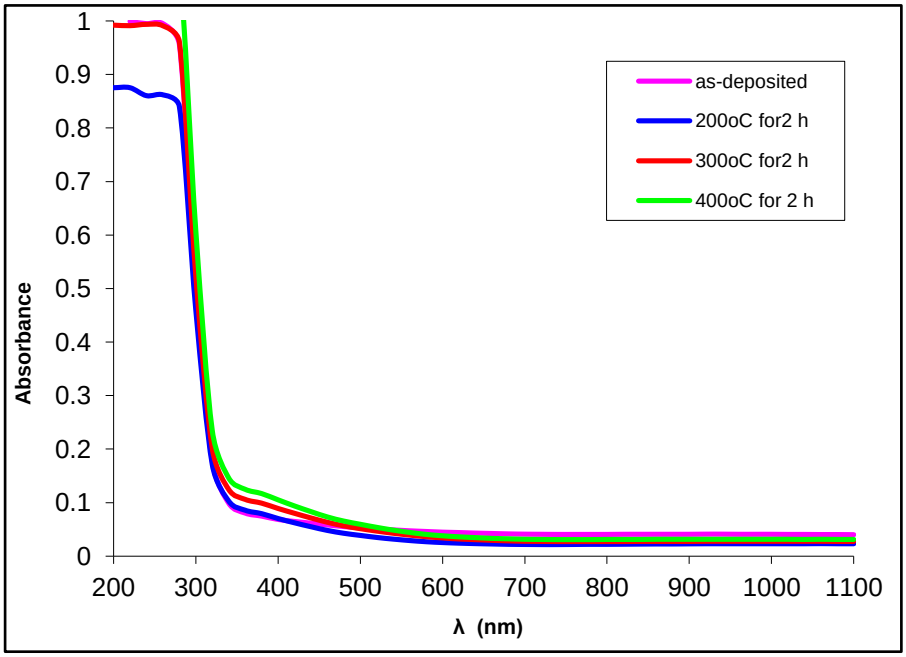

Fig.(4.19) Absorbance spectra of iron oxide nanofilm with different annealing temperature

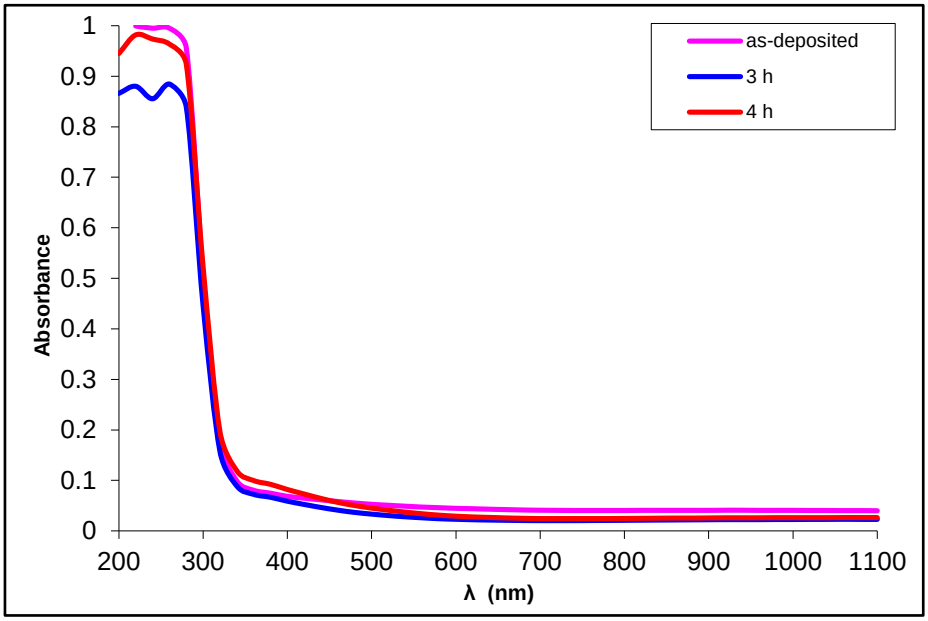

Fig.(4.20) Absorbance spectra of iron oxide nanofilm with different annealing time

4.4.2 Transmittance (T)

The transmittance spectra of Fe nanofilm as-deposited and different annealed temperature 200 ^{o}C , 300 ^{o}C and 400 ^{o}C for 2 hours as a function of wavelength are shown in figure (4.21) and different annealed time three and four hours for 200^{o}C as a function of wavelength are shown in figure (4. 22). From the figure (4.21), it is obtained that the transmittance reduce with increasing annealing temperature in the UV region and then increase with increasing annealing temperature in the visible and NIR regions, while in figure (4.22), the transmittance increase with increasing annealing time. This result is consistent with the findings of the researchers [93,94].

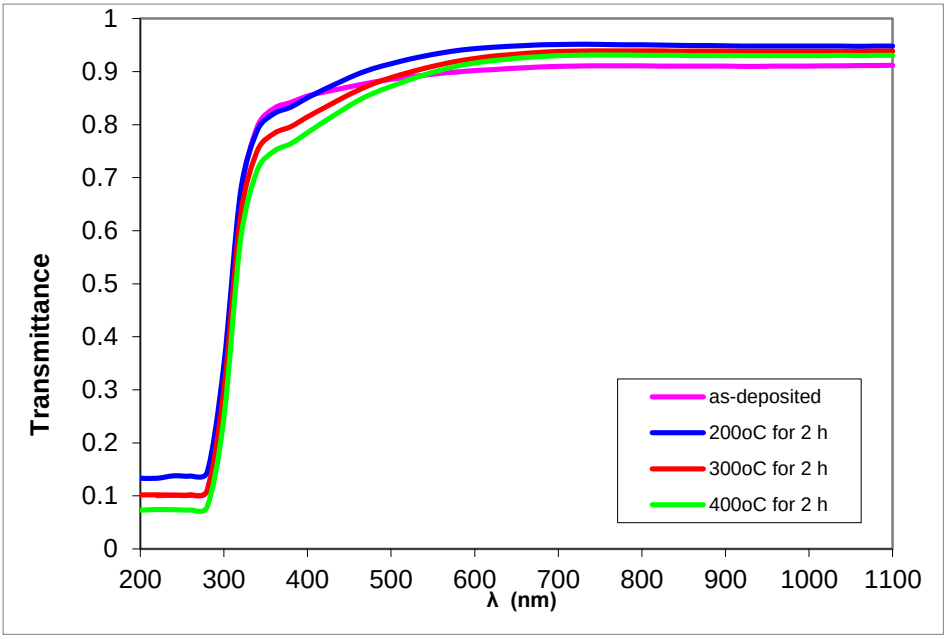

Fig.(4.21) Transmittance spectra of iron oxide nanofilm with different annealing temperature.

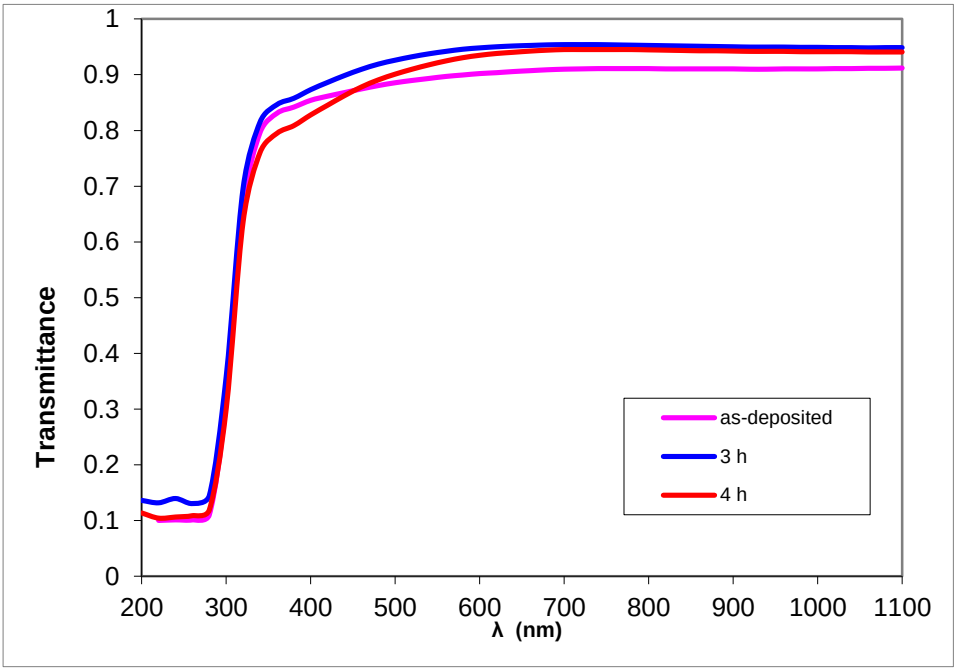

Fig.(4.22) Transmittance spectra of iron oxide nanofilm with different annealing time.

4.4.3 The absorption coefficient (α)

The absorption coefficient (α) has been calculated from the equation [2.8]. Figure (4.23) reveal to the absorption coefficient of as-deposited nanofilm and different annealed temperature at 200 °C 300 °C and 400 °C for 2 hours as a function of wavelength and different annealed time at 200°C for 3 and 4 hours as a function of wavelength are shown in figure (4.24). The value of α is greater than 10^4 cm^{-1} which mean the direct electron transition happen. From the figure (4.23), it is observed that the α increases with increasing annealing temperature in the UV region and then reduces with increasing annealing temperature in the visible and NIR regions, while in figure (4.24), the α decrease with increasing annealing time. This behaviour related to the absorbance. The absorption coefficient given the information on the transition nature.

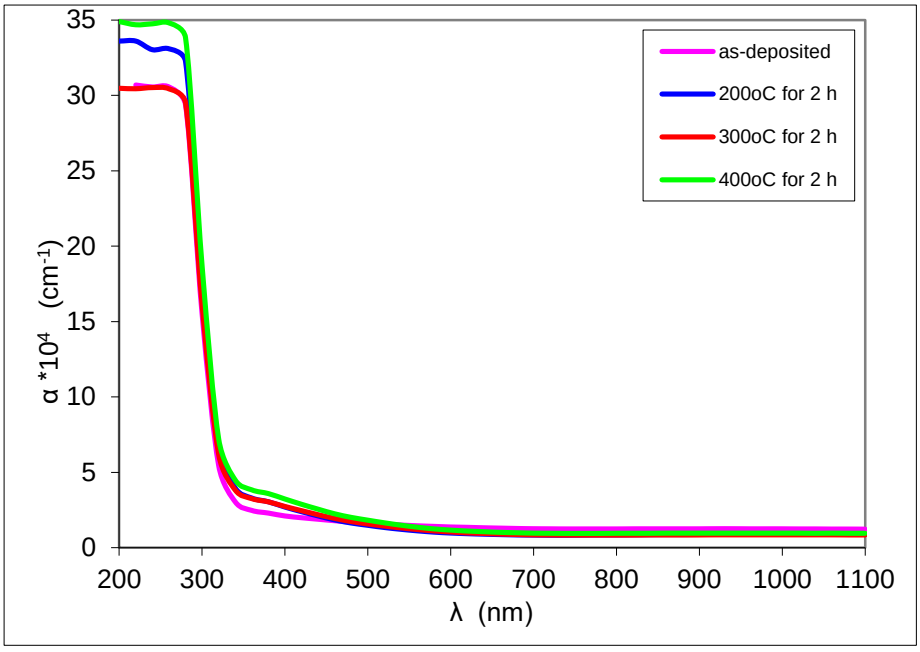

Fig.(4.23) Absorption coefficient of iron oxide film with different Annealing Temperature.

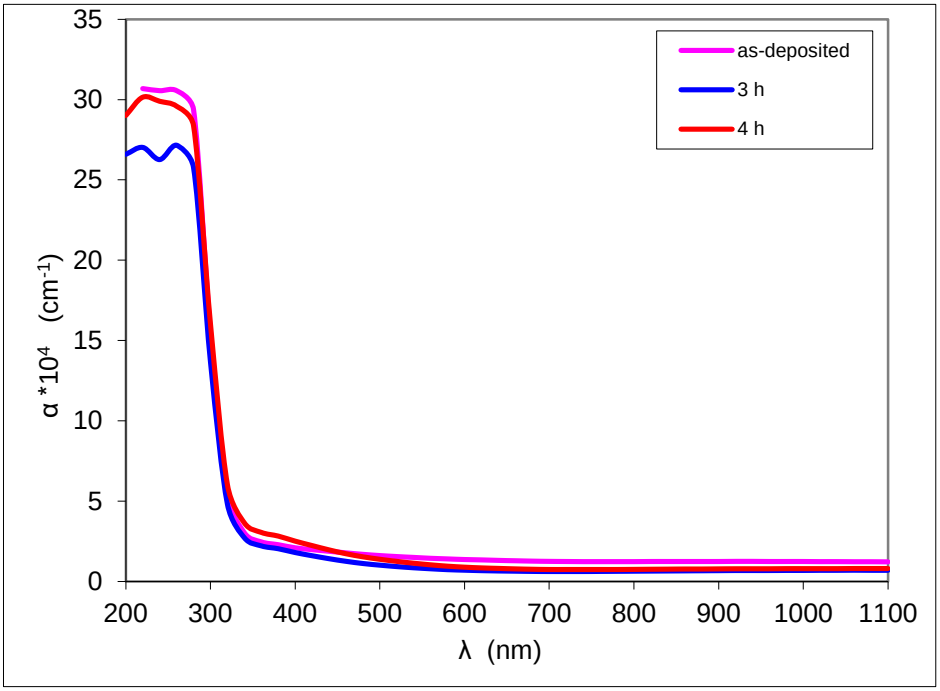

Fig.(4.24) Absorption coefficient of iron oxide film with different Annealing Time.

4.4.4 The Energy Gap

The direct optical energy gap (Eg^{opt}) of iron oxide nanofilms was calculated from equation (2.9). Figures 4.25and 4.26 explain the E_{gopt} of Fe nanofilm as-deposited and different annealed temperature at 200 ^{o}C 300 ^{o}C and 400 ^{o}C for 2 hours as a function of wavelength and different annealed time at 200^{o}C for 3 and 4 hours as a function of wavelength as a function of photon energy (hν) individually.

The plot of $(\alpha h\nu)^2$ against hν is linear in nature, indicating that the material of the nanofilms has a direct Eg^{opt}. The extrapolation of the straight line to α=0 gives a direct E_g^{opt} equal to 3.48 eV for the as-deposited nanofilms and this value reduce with increasing annealing temperature and takes the values 3.35, 3.39 and 3.31 eV at 200 ^{o}C, 300 ^{o}C and 400 ^{o}C for 2 hours respectively , as obtain in figure (4.25) and the E_g^{opt} reduce with increasing annealing time 3 and 4 hours for 200^{o}C and

takes the values 3.44 and 3.40 eV in figure (4.26), which is agree with report [93,94].

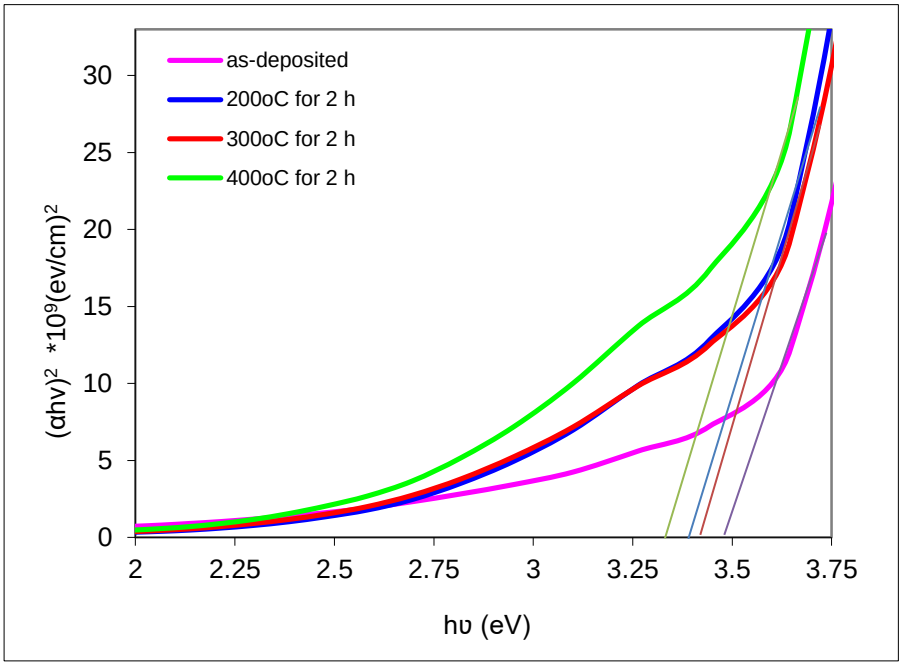

Fig.(4.25) Direct bad gap of iron oxide nanofilm with different annealing temperature.

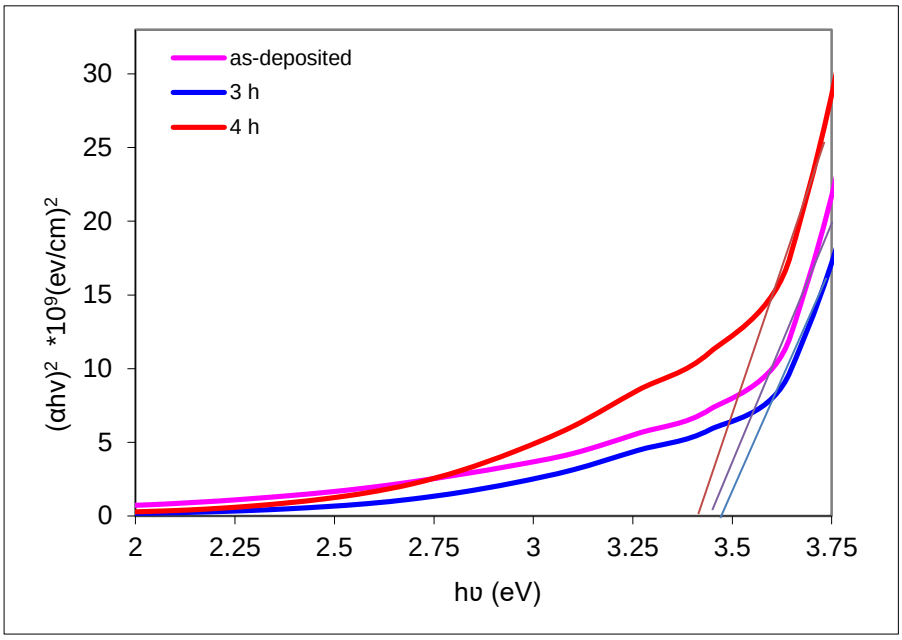

Fig.(4.26) Direct bad gap of iron oxide nanofilm with different annealing time.

Table (4.4): Value of the direct energy gap for all the Fe nanofilms with different annealing temperature.

Different annealing temperature	Optical energy gap (eV)
As-deposited	3.48
200^{o}C for 2h	3.35
300^{o}C for 2h	3.39
400^{o}C for 2h	3.31

Table (4.5): Value of the direct energy gap for all the Fe nanofilms with different annealing time.

Different annealing time	Optical energy gap (eV)
As-deposited	3.48
200^{o}C for 3h	3.47
200^{o}C for 4h	3.40

4.4.5 The refractive index (n)

The refractive index (n) was calculated from equation (2-13). Figures 4.27 and 4.28 explain the refractive index of Fe nanofilm as-deposited and different annealed temperature 200 ^{o}C, 300 ^{o}C and 400 ^{o}C for 2 hours and different annealed time at 200^{o}C for 3 and 4 hours as a function of wavelength individually. From this figures, it is obtain that the n decrease with increasing annealing temperature and time individually. This behaviour due to the decrease in density of nanofilms with increasing annealing temperature and time.

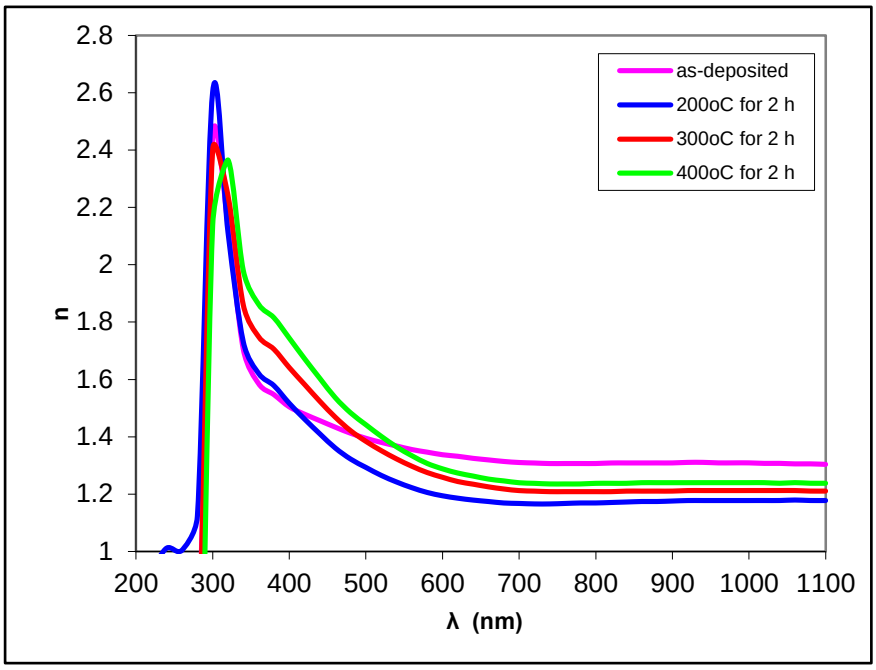

Fig.(4.27) Refractive index of iron oxide nanofilm with different annealing temperature.

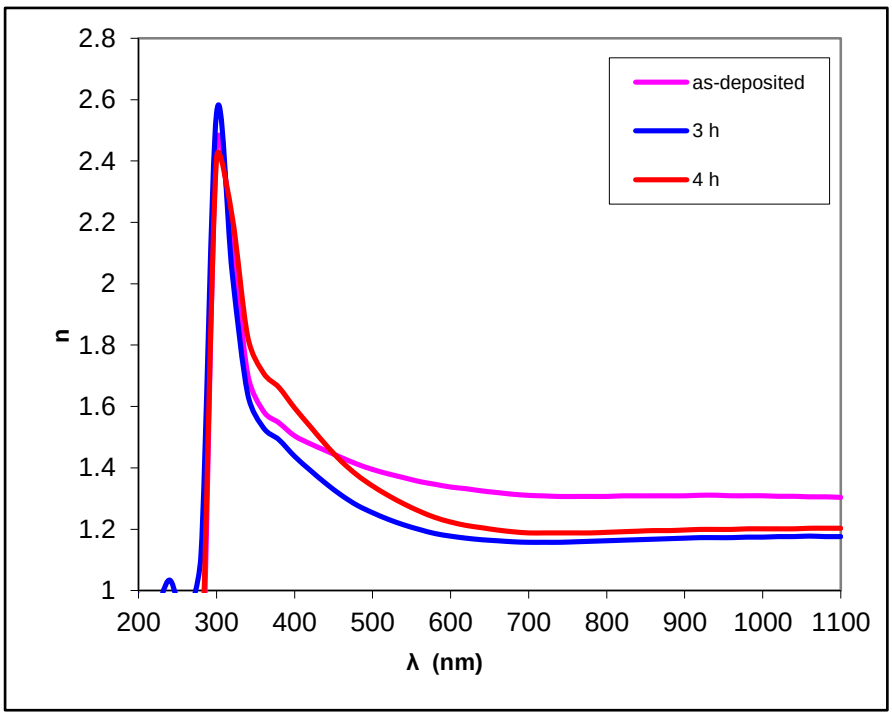

Fig.(4.28) Refractive index of iron oxide nanofilm with different annealing time.

4.4.6 The extinction coefficient (k)

The extinction coefficient (k) was calculated from equation (2.15). Figures 4.29 and 4.30 explain the extinction coefficient of Fe nanofilm as-deposited and different annealed temperature 200 ^{o}C, 300 ^{o}C and 400 ^{o}C for 2 hours and different annealed time three and four hours for 200^{o}C as a function of wavelength individually. From the figure (4.29), it is obtain that the k increases with increasing annealing temperature in the UV region and then reduces with increasing annealing temperature in the visible and NIR regions, while in figure (4.30), the k decrease with increasing annealing time. This behaviour explained by the fact that the k has a similar behaviour to the absorption coefficient.

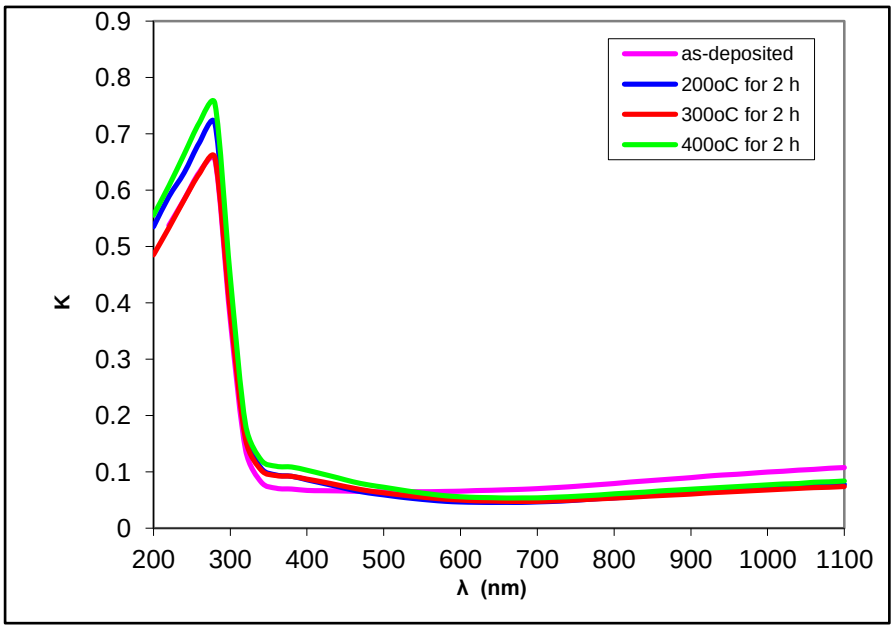

Fig.(4.29) Extenction coefficient of iron oxide nanofilm with different annealing temperature.

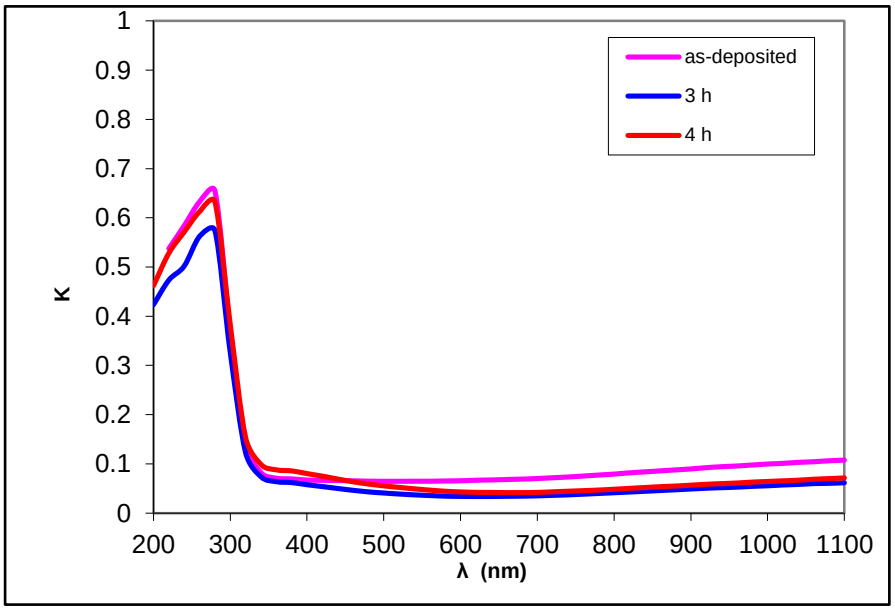

Fig.(4. 30) Extinction coefficient of iron oxide nanofilm with different annealing time.

The real and imaginary parts of dielectric constant are calculated by using equations(2.17) and (2.18) respectively. Figures (4.31-4.34) explain the real and imaginary parts of dielectric constant of Fe nanofilm as-deposited and different annealed temperature 200 ^{o}C, 300 ^{o}C and 400 ^{o}C for 2 hours and different annealed time three and four hours for 200^{o}C as a function of wavelength individually. From the figures 4.31 and 4.33, it is obtain that the real parts of dielectric constant decrease with increasing annealing temperature and time individually. This is due to the real part of dielectric constant depends on refractive index because the effect of extinction coefficient is very small. Figure (4.32) explain the imaginary part of dielectric constant increases with increasing annealing temperature in the UV region and then reduces with increasing annealing temperature in the visible and NIR regions, while in figure (4.34), the imaginary part decrease with increasing annealing time because the imaginary part of dielectric constant depends on extinction coefficient especially in the

visible and NIR regions of wavelength where the refractive index is approximately constant while extinction coefficient increases with the increase of the wavelength [94].

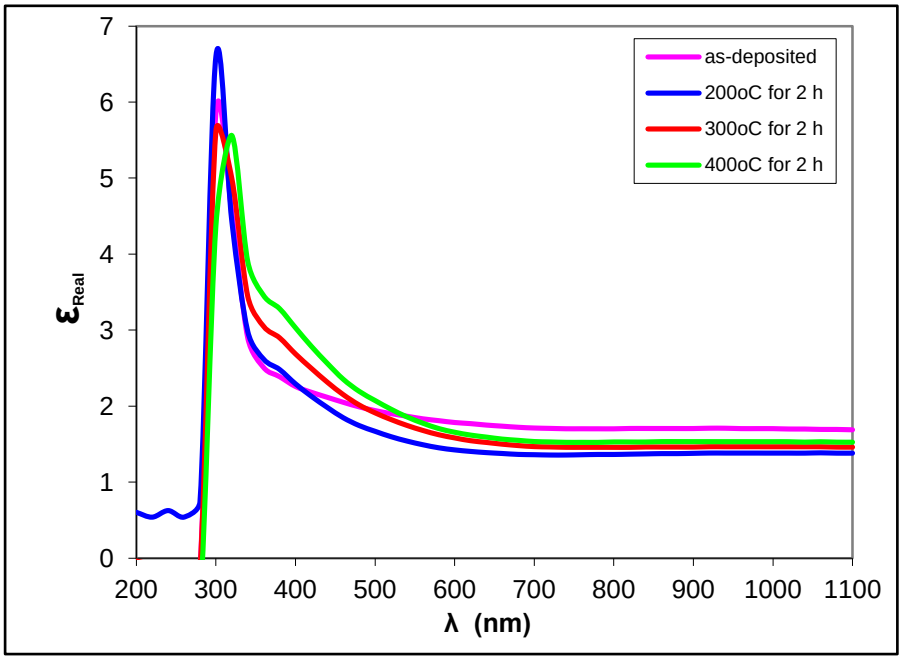

Fig.(4.31) Real parts of dielectric constant of iron oxide nanofilm with different annealing temperature.

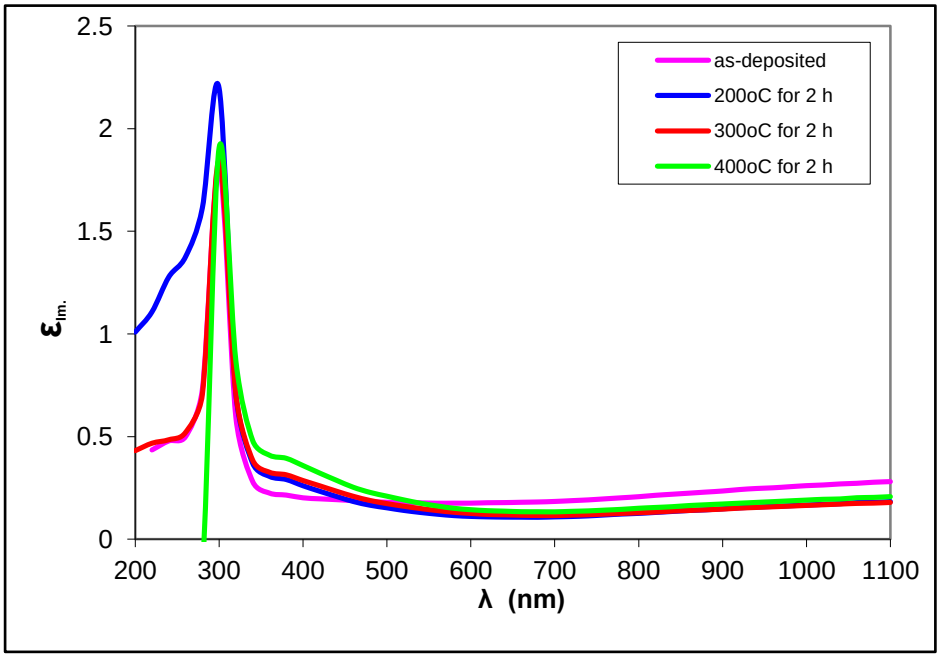

Fig.(4.32) Imaginary parts of dielectric constant of iron oxide nanofilm with different annealing temperature

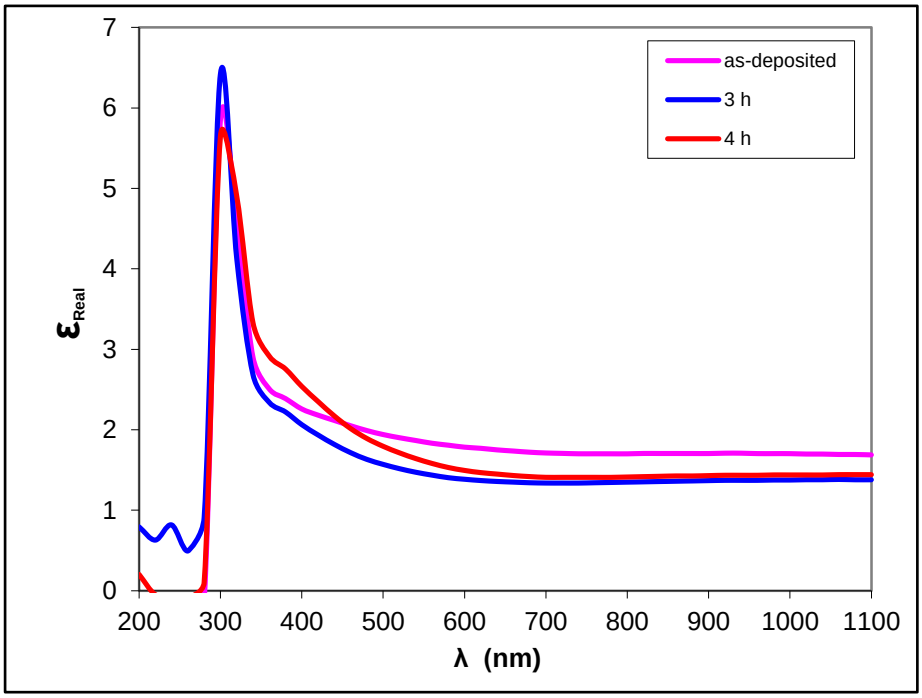

Fig.(4.33) Real parts of dielectric constant of iron oxide nanofilm with different annealing time.

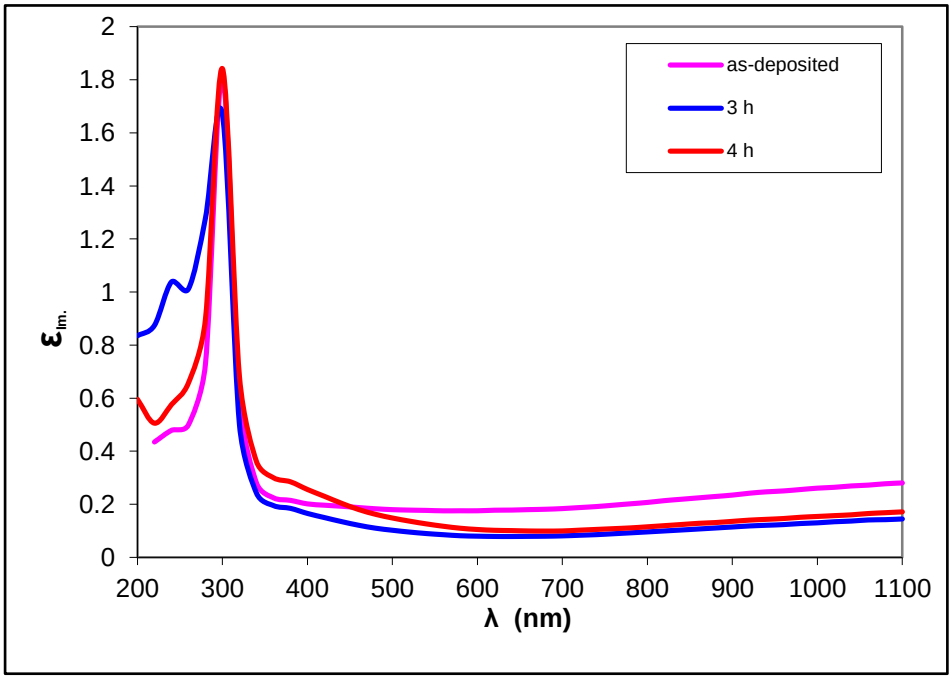

Fig.(4.34) Imaginary parts of dielectric constant of iron oxide nanofilm with different annealing time.

4-5 Conclusion

From preparing pure iron nanofilms deposited on glass substrates with different annealing temperature of 200^{o}C, 300^{o}C and 400^{o}C and different annealing time at 200°C for 3 and 4 hours by thermal evaporation technique, it can be concluded:

1. The characterization of the samples by XRD (X-ray diffraction) confirmed the formation of mixed phases of iron oxide hematite (α-Fe_2O_3) and maghemite (γ-Fe_2O_3) from Fe at annealing at different temperature and time in the presence of air.

2. The values of the average particle size of the oxidation mixed phases (hematite α-Fe_2O_3 and maghemite γ-Fe_2O_3) deduced from SEM micrographs and their corresponding XRD agree reasonably well, thus indicating a high degree of crystallinity.

3.The SEM images showed that the flower-like clusters of Fe2O3 nanoparticles spread on the surface of the annealed film at a temperature of 200 for 2 and 3 hours, and also in the form of layers for annealing in 4 hours, which are a candidate for energy storage applications.

3. The AFM images of iron oxide nanofilms show a high surface homogeneity in which the distribution of crystalline granules is uniform which is evident from the convergence of the roughness and root mean square (RMS) values.

5. The optical properties results show that the absorbance increases with increasing annealing temperature in the UV region and then reduces with increasing the annealing temperature in the visible and NIR regions,

whereas, the absorbance decrease with increasing annealing time, while the transmittance reduce with increasing annealing temperature in the UV region and then increase with increasing annealing temperature in the visible and NIR regions whereas, the transmittance increase with increasing annealing time

6.The optical measurement shows that the Fe nanofilms have allowed direct energy gap (E_g^{opt}). The E_g^{opt} decreased with increasing annealing temperature and time respectively. It is decreased from 3.48 eV as-deposited to 3.33 eV at 400 ^oC for 2 hours and to 3.40 eV at 200^oC for 4 hours.

7. The optical constants such as absorption coefficient, extinction coefficient and imaginary parts of dielectric constant increased with increasing annealing temperature in the UV region and then reduces with increasing annealing temperature in the visible and NIR regions, while these optical constant decreased with increasing annealing time. refractive index and real parts of dielectric constant decreased with increasing annealing temperature and time.

4.6 Suggestions for Future Work

1. Preparing the Fe nanofilms by thermal evaporation technique with other different annealing temperature and time.

2. Use these result to apply at different application such as energy storage and solar cell.

3. Preparing the Fe nanofilms by chemical vapour deposition technique

References

References

1. K. L. Chopra, "Thin film devices application", Plenum press, New York, 1983.
2. K. L. Chopra, "Thin films phenomena", Mc. Graw-Hill, NewYork, 1969.
3. L. Eckortova, "Physics of thin films", Plenum press, 1977.
4. R. H. Bossert, C. J. Tool, J. A. Roosmalen, C. H. Wentink, and M. J. Devaan, "Thin-Film Solar Cells", Technology Evaluation and Perspectives, Netherlands Energy Research Foundation – ECN, (2000).
5. Pepperhoff, Werner, and Mehmet Acet. "The structure of iron." Constitution and Magnetism of Iron and its Alloys. Springer, Berlin, Heidelberg, 2001. 1-13.
6. Wu W, He Q G and Jiang C Z Magnetic iron oxide nanoparticles: synthesis and surface functionalization strategies Nanoscale Res. Lett. 3 397, 2008.
7. Gupta A K and Gupta M 2005 Synthesis and surface engineering of iron oxide nanoparticles for biomedical applications Biomater. 26 3995
8. Gilchrist R, Medal R, Shorey W D, Hanselman R C, Parrott J C and Taylor C B 1957 Selective inductive heating of lymph nodes Ann. Surg. 146 596
9. Cornell RM. *et al.*, " The iron oxides: structure, properties, reactions, occurrences and uses ", 2003.
10. Zhu K. et al., " Magnetic Nano materials: chemical design, synthesis and potential applications ", Acc Chem Res., Vol.51, 2018.
11. Boris IK. *et al.*, "Iron-containing nanomaterials: synthesis, properties, and environ- mental applications", RSC Adv.,Vol. 2, (2012).
12. Cordova G. et al., "Force Microscopy Characterization of Super paramagnetic Iron Oxide Nanoparticles (SPIONs)", Nano BioMed ENG., Vol.6, No.1), pp.(31-39), (2014).
13. Hasany S. *et al* ., "Magnetic Iron Oxide Nanoparticles: Chemical Synthesis and Applications", Review. CNANO., Vol. 9, No.5, pp.(561- 575), (2013).
14. Xie J., Jon S., " Magnetic Nanoparticle – Based Theranostics", Theranostics, Vol.2, No. 1, pp.(122-124), (2012).

15. Laurent S. *et al.*, " Magnetic Iron Oxide Nanoparticles: Synthesis, Stabilization, Vectorization, Physicochemical Characterizations, and Biological Applications", Chem. Rev., Vol. 108, No.6, pp.(2064-2110), (2008).
16. Buschow, K.H.G. ed., "Hand Book of Magnetic Materials", Elsevier, (2006).
17. Lu A H, Salabas E L and Schuth F, "Magnetic nanoparticles: synthesis, protection, functionalization, and application Angew. Chem". Int. Edn 46 1222, 2007.
18. Massart R "Preparation of aqueous magnetic liquids in alkaline and acidic media" IEEE Trans. Magn. 17 1247, 1981.
19. Park J, An K, Hwang Y, Park J G, Noh H J, Kim J Y، Park J H, Hwang N M and Hyeon T, "Ultra-large-scale syntheses of monodisperse nanocrystals Nat". Mater. 3 891, 2004.
20. Ma J, Lian J, Duan X, Liu X and Zheng W, "α-Fe2O3: Hydrothermal synthesis, magnetic and electrochemical properties", J. Phys. Chem. C 114 10671, 2010.
21. Qi H, Yan B, Lu W, Li C and Yang Y A, "non-alkoxide sol-gel method for the preparation of magnetite (Fe_3O_4)nanoparticles Curr. Nanosci". 7 381, 2011.
22. Okoli C, Boutonnet M, Mariey L, Järås S and Rajarao G , "Application of magnetic iron oxide nanoparticles prepared from microemulsions for protein purification", J. Chem. Technol. Biot. 86 1386, 2011.
23. Zhu S, Guo J, Dong J, Cui Z, Lu T, Zhu C, Zhang D and Ma J, "Sonochemical fabrication of Fe3O4 nanoparticles on reduced graphene oxide for biosensors Ultrason". Sonochem. 20 872, 2013.
24. Jiang F Y, Wang C M, Fu Y and Liu R C, Synthesis of iron oxide nanocubes via microwave-assisted solvolthermal method J. Alloys Compd. 503 L31, 2010.
25. Sundaram P A, Augustine R and Kannan M, "Extracellular biosynthesis of iron oxide nanoparticles by Bacillus subtilis strains isolated from rhizosphere soil Biotechnol". Bioprocess Eng. 17 835, 2012.

26. Pascal C, Pascal J L, Favier F, Elidrissi Moubtassim M L and Payen C, "Electrochemical synthesis for the control of γ-Fe2O3 nanoparticle size: morphology, microstructure, and magnetic behavior Chem". Mater. 11 141, 1998.
27. Huang H Y, Shieh Y T, Shih C M and Twu Y K, "Magnetic chitosan/iron (II, III) oxide nanoparticles prepared by spray-drying Carbohydr". Polym. 81 906, 2010.
28. Salazar-Alvarez G, Muhammed M and Zagorodni A A, "Novel flow injection synthesis of iron oxide nanoparticles with narrow size distribution Chem". Eng. Sci. 61 4625, 2006.
29. Moaca E.A. *et al.*, " Preclinical aspects on magnetic iron oxide nanoparticles and their interventions as anticancer agents: enucleation, apoptosis and other mechanism", Iron Ores Iron Oxide Mater., 2018.
30. Machala L. et al., "Polymorphous transformations of nanometric iron (III) oxide", a review. Chem Mater, Vol. 23, No.14., pp.(3255-3272), 2011.
31. mohammad A. *et al.*, " Optical properties of iron oxide (α-Fe 2O 3) thin films deposited by the reactive evaporation of iron", Journal of Alloys and Compounds, Vol.521, pp. (178-182), 2012.
32. Yucheng D. et al., " Thermal evaporation-induced anhydrous synthesis of Fe3O4–graphene composite with enhanced rate performance and cyclic stability for lithium ion batteries ", Phys. Chem. Chem. Phys, Vol.15, pp.(7174—7181), (2013).
33. Eunice A. Campos. *et al.*, "Synthesis, Characterization and Applications of Iron Oxide Nanoparticles ", Journal of Aerospace Technology and Management, Vol. 7, No.3,pp. (267-276), 2015.
34. Kostyukova, D., & Chung, Y. H, "Synthesis of iron oxide nanoparticles using isobutanol". Journal of Nanomaterials, 2016.
35. Yazirin, C., Puspitasari, P., Sasongko, M. I. N., Tsamroh, D. I., & Risdanareni, P. "Phase identification and morphology study of hematite (Fe_2O_3) with sintering time varitions" In AIP Conference Proceedings, Vol. 1887, No. 1, p. 020038, 2017.

36. Suturin, S. M., *et al*. "Tunable polymorphism of epitaxial iron oxides in the four-in-one ferroic-on-GaN system with magnetically ordered α-, γ-, ε−Fe $_2$O $_3$, and Fe $_3$O$_4$ layers" Physical Review Materials 2.7 , 073403, (2018).

37. Natarajan. *et al.,* "Multifunctional magnetic iron oxide nanoparticles: diverse synthetic approaches, surface modifcations, cytotoxicity towards biomedical and industrial applications ", BMC Materials Journal, Vol.1, No.2, pp. (1-22), 201).
38. Coduri, M., Masala, P., Del Bianco, L., Spizzo, F., Ceresoli, D., Castellano, C., ... & Scavini, M. Local structure and magnetism of Fe2O3 maghemite nanocrystals: The role of crystal dimension. *Nanomaterials*, *10*(5), 867, 2020.
39. Khadayeir, A. A., Wannas, A. H., & Yousif, F. H. Effect of Applying Cold Plasma on Structural, Antibacterial and Self Cleaning Properties of α-Fe2O3 (HEMATITE) Thin Film. *Emerging Science Journal*, *6*(1), 75-85, 2022.
40. Sidra Farooq, Saira Riaz, and Shahzad Naseem" Thermally Evaporated Fe-Ox Thin Films for use in MTJs – Structural, Magnetic and Electrical Properties", Advances in Civil, Environmental, and Materials Research (ACEM' 12) Seoul, Korea, August 26-30, 2012
41. Ghosh, R., D. Basak, and Shinobu Fujihara. "Effect of substrate-induced strain on the structural, electrical, and optical properties of polycrystalline ZnO thin films." Journal of Applied Physics 96.5: 2689-2692, 2004.
42. Wu W, Xiao X H, Zhang S F, Zhou J A, Fan L X, Ren F and Jiang C Z "Large-scale and controlled synthesis of iron oxide magnetic short nanotubes: shape evolution, growth mechanism, and magnetic properties". J. Phys. Chem. C 114 16092, 2010.
43. Zhang Z, Boxall C and Kelsall G H "Photoelectrophoresis of colloidal iron oxides": 1. Hematite (α-Fe2O3) Colloids Surf. A 73 145, 1993.
44. Boxall C, Kelsall G and Zhang Z, "Photoelectrophoresis of colloidal iron oxides. Part 2—magnetite (Fe3O4)", J. Chem. Soc. Faraday Trans. 92 791, 1996.

45. Martínez G, Malumbres A, Mallada R, Hueso J, Irusta S, Bomatí-Miguel O and Santamaría J, "Use of a polyol liquid collection medium to obtain ultrasmall magnetic nanoparticles by laser pyrolysis Nanotechnology" 23, 425605, 2012.
46. Teja, Amyn S., and Pei-Yoong Koh. "Synthesis, properties, and applications of magnetic iron oxide nanoparticles." Progress in crystal growth and characterization of materials 55.1-2: 22-45, 2009.
47. Sadri R., "A facile, bio-based, novel approach for synthesis of covalently functionalized graphene nanoplatelet nano-coolants toward improved thermo-physical and heat transfer properties", Journal of Colloid and Interface Science, Vol.509, pp.(140–152), 2018.
48. Hubler A. and Osuagwu O., "Digital quantum batteries: Energy and information storage in nanovacuum tube arrays". Complexity: NA, 2010.
49. Portela Carlos M, et al., "Extreme mechanical resilience of self-assembled nanolabyrinthine materials". Proceedings of the National Academy of Sciences, Vol.117, No.11, pp. (5686–5693), 2020.
50. Eldridge T., "Achieving industry integration with nanomaterials through financial markets", Nanotechnology_Now, 2014.
51. McGovern C., "Commoditization ofnanomaterials", Nanotechnol. Perceptions, Vol.6 No.3, pp.(155-178), 2010.
52. Wang X. et al., "Biomimetic Nanoceramic in Clinical Use: From Materials to Applications", Advanced Materials, vol. 18, pp. (2031-2034), 2006.
53. Liu J. et al, "Preparation of durable superhydrophobic surface by sol–gel method with water glass and citric acid", Journal of Sol-gel Science and Technology, Vol. 58, No. 1, 2011.
54. Pokropivny V. et al, "Introduction to Nanomaterials and Nanotechnology" , Tartu University Press, pp. (45-100), 2007.
55. Jaeger Richard C.,"Film Deposition Introduction to Microelectronic Fabrication", (2nd ed.), Upper Saddle River: Prentice Hall. 2002.
56. Metha A., "Principle". PharmaXChange.info.Inc., New York., 1971.

57. Archi Dasgupta, Lakshmy PulickalRajukumar, ChristopherRotella, YuLei, MauricioTerrones, " Covalent three-dimensional networks of graphene and carbon nanotubes: synthesis and environmental applications" Journal of NanoToday, Pages 116-135, February, Volume 12,2017 .
58. Roberto Alicandro, Lucia De Luca, Adriana Garroni, and Marcello Ponsiglione, "Metastability and dynamics of discrete topological singularities in twodimensions: a -convergence approach", Archive for Rational Mechanics and Analysis, Vol. 214, No. 1, 2014.
59. Hillel Aharoni, Thomas Machon, and Randall Kamien, Composite dislocations in smectic liquid crystals, Physical review letters, Vol. 118, No.25 ,2017.
60. Amit Acharya and Xiaohan Zhang, From dislocation motion to an additive velocity gradient decomposition, and some simple models of dislocation dynamics, Chinese Annals of Mathematics, Series B 36B, Vol.645, No.5, 2015.
61. R. O. Gould and W. Massa, Crystal Structure Determination. Springer Berlin Heidelberg,(2013).
62. Luana Tortora and Oleg D. Lavrentovich, Chiral symmetry breaking by spatial con_nement in tactoidal droplets of lyotropic chromonic liquid crystals, Proceedings of the National Academy of Sciences, Vol. 108, No.13, 2011.
63. Luana Tortora, Heung-Shik Park, Shin-Woong Kang, Victoria Savaryn, Seung-Ho Hong, Konstantine Kaznatcheev, Daniele Finotello, Samuel Sprunt, Satyendra Kumar, and Oleg D. Lavrentovich, Self-assembly, condensation, and order in aqueous lyotropic chromonic liquid crystals crowded with additives, Soft Matter, Vol. 6 ,2010.
64. Tanmay Vachaspati, Formation of topological defects, Physical Review, No.12, 1991.
65. A. J. Vattr_e and M. J. Demkowicz, Determining the Burgers vectors and elastic strain energies of interface dislocation arrays using anisotropic elasticity theory, Acta Materialia, Vol.61, No.14, 2013.
66. Fox M., "Quantum optics; an introduction", Oxford University, Press, 2006.

67. Guinier A., "X-ray diffraction in crystals, imperfect crystals, and amorphous bodies", Freeman, San Francisco, 1963.
68. Als-Nielsen J. and McMorrow D., "Elements of modern X-ray physics", John Wiley and Sons, Ltd., Chichester, 2001.
69. Barrett C. S. and Massalski T.B.," Structure of Metals", Mc Graw-Hill, New York, 1966.
70. Singh A. et al.," Effect of Post Annealing Temperature on Structural and Optical Properties of ZnCdO Thin Films Deposited by Sol–Gel Method", Applied Surface Science, Vol.258No.5, pp. (1881-1887), 2011.
71. Yousif A., "Structural, Morphological, photo-Properties of Hetrojunction ZnO Nanostructure Films Deposited on n-Si(100)by PLD", IJAIEM,Vol.3, pp. (44- 55), 2014.
72. Moharram H. et al., "Direct Precipitation and Characterization of ZnO Nanoparticles", Journal of Nanomaterials, 2014.
73. Singh A. and Kumar P., "Structural, morphological and optical properties of sol-gel processed CdZnO nanostructured films: effect of precursor solvents", International Nano Letters, Vol.3, No.1, pp. (1- 6), 2013.
74. Efros A. and Shklovskii B. I., "Critical Behaviour of Conductivity and Dielectric Constant Near the Metal-Non-Metal Transition Threshold", Physical Status Solid (b), Vol.76, No.2, pp. (475-485), 1976.
75. vashchenko I. and Kerner I. , "Physical Approaches to Improvement of Semiconductor Gas Sensor Based on SnO2 Thin Films", Moldavian Journal. of the Physical Sciences, No.1, pp. (95-102), 2003.
76. Allen T. et al., "Scanning Probe and Scanning Electron Microscopy", Elsevier Science (USA), 2006.
77. Dunlap M. and Adaskaveg J. E., "Introduction to the Scanning Electron Microscope", Facility for Advanced Instrumention, 1997.
78. Meyer E., "Atomic force microscopy", Progress in Surface Science, Vol. 41, pp. (3-49), 1992.

79. Said A. et al., " Synthesis of nanohybrid materials by femtosecond laser ablation in liquid medium", IOP Publishing J. of Physics: Conference Series, No.59, pp. (259-265), 2007.
80. Pankove J., "Optical processes in semiconductors", Prentice– Hall, Inc., Englewood Cliffs, Vol. 285, pp. (111), 1971.
81. Barranco A. et al., "Perspectives on oblique angle deposition of thin films: from fundamentals to devices", Journal of Progress in Materials Science, Vol. 76, pp. (59-153), 2016.
82. K. L. Chopra, S. Major, and D. K. Pandya, Thin Solid Films, 102 (1): p. 1, 1983 .
83. Newman D., "Semiconductor physics and devices", Basis Principles, Richard, University of New Mexico, Vol. 435, pp.211, 199).
84. Millman J., "Microelectronics", Murray–Hill, Book Company Kogakusha, Vol. 642, pp.172, 1979.
85. Elliot R. and Gibson A.I.,"An introduction to solid state physics and application", Macillian Inc., Vol. 471, pp.92, 1974.
86. Kazmarski L. and Clark A., "Polycrystalline and amorphouse thin films and device", Edited by Lawrence Academic Press, New York, Vol. 267, pp.142, 1980.
87. Taus J., "Amorphous and liquid semiconductor", Plenums Press, New York and London, Vol. 271, pp. 99, 1974.
88. Stenzel O., "The physics of thin film optical spectra", Springer Series in Surface Sciences, Vol 978, pp. (214-220), 2015.
89. Gumus C. et al., "Structural and optical properties of zinc oxide thin films prepared by spray pyrolysis method", J. Optoelectronics and Advanced Materials, 2006.
90. S. Akarapu, H. Zbib, and J. P. Hirth, Modeling and analysis of disconnections in tilt walls, Scripta Materialia, Vol.59, No.3, 2008.
91. Sze S.M., "Semiconductor Devices: Physics and Technology" , 2001.
92. Mathis R. D., "Company Evaporation Sources Catalog", pp.(1-7) and pp. (12), 1992.

93. Meftah, Y., et al. "Post annealing effect on structural and optical properties of (α-Fe2O3) thin films prepared by spray pyrolysis with moving nozzle." Digest Journal of Nanomaterials and Biostructures 13.2: 465-474, 2018.

94. Ferdous, Zannatul, Md Samir Ullah, and Sabina Hussain. "Temperature and Substrate Effects on the Structural, Morphological, and Optical Properties of Iron Oxide Thin Films Prepared by Spray Pyrolysis Technique." Dhaka University Journal of Science 68.1, 79-85, 2020.

الخلاصة

في هذه الدراسة ، تم استخدام تقنية التبخير الحراري لتحضير أغشية نانوية من الحديد (Fe) المترسبة على ركائز زجاجية بدرجات حرارة تلدين مختلفة تبلغ 200 درجة مئوية و 300 درجة مئوية و 400 درجة مئوية وزمن تلدين مختلف عند 200 درجة مئوية لمدة 3 و 4 ساعات عن طريق التبخير الحراري. من تحليلات حيود الأشعة السينية (XRD) أقرت بتكوين طور الهيماتيت لهيكل رباعي الزوايا البلوري (γ-Fe2O3) والهيكل البلوري السداسي الماغيميت (α-Fe2O3). التلدين عند درجات حرارة وزمن مختلفين في وجود الهواء يؤدي إلى الأكسدة ويكشف عن الأطوار المختلطة لأكسيد الحديد الماغيميت والهيماتيت. زاد معدل الحجم البلوري للأغشية النانوية الحديدية مع زيادة درجة حرارة التلدين والوقت. زاد من 15.12 نانومتر بدون تلدين إلى 21.67 نانومتر ملدن عند 200 درجة مئوية لمدة 4 ساعات. تُظهر صور مجهر القوة الذرية (AFM) لأغشية نانوية لأكسيد الحديد تجانسًا عاليًا للسطح يكون فيه توزيع الحبيبات البلورية منتظمًا وهو ما يتضح من تقارب قيم الخشونة والجذر المتوسط التربيعي (RMS). تمت زيادة قيم الخشونة والجذر المتوسط التربيعي (RMS) من 1.1 نانومتر و 1.43 نانومتر بدون تلدين إلى 8.35 نانومتر و 10.6 نانومتر الملدن عند 200 درجة مئوية لمدة 4 ساعات. أظهرت صور المجهر الإلكتروني الماسح (SEM) أن تجمعات الجسيمات النانوية على شكل أزهار تنتشر على السطح ، والتي ظهرت في جميع العينات المرسبة على قواعد زجاجية، خاصة عند درجة حرارة 200 درجة مئوية. أظهرت نتائج الخصائص البصرية أن الامتصاصية تزداد مع زيادة درجة حرارة التلدين في منطقة الأشعة فوق البنفسجية ثم تنخفض مع زيادة درجة حرارة التلدين في المناطق المرئية و NIR ، بينما تقل النفاذية مع زيادة وقت التلدين ، بينما تقل النفاذية مع زيادة درجة حرارة التلدين في منطقة الأشعة فوق البنفسجية ثم تزداد مع زيادة درجة حرارة التلدين في المناطق المرئية و NIR. يُظهر القياس البصري أن أغشية الحديد النانوية سمحت بفجوة طاقة مباشرة .تتناقص فجوة الطاقة مع زيادة درجة حرارة التلدين والوقت على التوالي. تنخفض من 3.48 فولت بدون تلدين إلى 3.33 فولت عند 400 درجة مئوية لمدة ساعتين ومن 3.48 فولت بدون تلدين إلى 3.40 فولت عند 4 ساعات مقابل 200 درجة مئوية. كما تم دراسة الثوابت البصرية مثل معامل الامتصاص ومعامل الخمود ومعامل الانكسار والجزء الحقيقي والخيالي لثابت العزل الكهربائي.

جمهورية العراق
وزارة التعليم العـــالي والبحث العلـمي
جامـــعة بابـــل
كليـــة التربية للعـــلوم الصرفة
قســـم الفيزيـــاء

تصنيع أغشية أوكسيد الحديد النانوية من الحديد المبخر حرارياً بعد المعاملة الحرارية: التركيب و الخصائص البصرية

رسالة مقدمة
إلى مجلس كلية التربية للعلوم الصرفة في جامعة بابل
وهي جزء من متطلبات نيل درجة الماجستير في التربية/الفيزياء

من قبل

شيماء عبد العالي مخيف عبيس

بكالوريوس تربية (علوم الفيزياء)
جامعة بابل 1999 م

بأشراف

أ. د. فؤاد شاكر هاشم **أ. د. خالد حنين عباس**

1443 هـ **2022 م**